Role of contrast of a relativistic femtosecond laser pulse interacting with solid and structured targets

K.A. Ivanov, S.A. Shulyapov, D.A. Gorlova, I.M. Mordvintsev, I.N. Tsymbalov, A.B. Savel'ev

Contents

Abstract. We consider the effect of a pre-plasma layer inevitably present in experiments on the acceleration of electrons and ions during interaction of a relativistic femtosecond laser pulse with a dense plasma. The interaction regimes are identified in which the presence of such a layer can significantly increase the average and maximum energies of electrons. The regimes are discussed in which an artificial nanosecond prepulse makes it possible to produce a collimated electron beam with a high charge and an average energy of up to 10 ponderomotive energies in the direction of the reflected or incident laser beam. It is shown that the acceleration of ions, as a rule, requires an ultrahigh contrast of the laser pulse, since the parameters of the accelerated ion beams deteriorate significantly in the presence of preplasma or due to the evaporation of a thin-film target. The regimes of interaction of laser pulses with thick targets, in which heavy multiply charged ions can be accelerated by cleaning the surface with a prepulse, are also discussed. An essential part of the review is devoted to the interaction of radiation with micro- and nanostructured targets. Both the methods of their fabrication and the issues related to the interaction of a femtosecond laser pulse and its contrast with such structures are considered.

K.A. Ivanov, I.M. Mordvintsev, A.B. Savel'ev Faculty of Physics, Lomonosov Moscow State University, Vorob'evy gory 1, stroenie 2, 119991 Moscow, Russia; Lebedev Physical Institute, Russian Academy of Sciences, Leninsky prosp. 53, 119991 Moscow, Russia;
S.A. Shulyapov Faculty of Physics, Lomonosov Moscow State University, Vorob'evy gory 1, stroenie 2, 119991 Moscow, Russia;
D.A. Gorlova, I.N. Tsymbalov Faculty of Physics, Lomonosov Moscow State University, Vorob'evy gory 1, stroenie 2, 119991 Moscow, Russia; Institute for Nuclear Research, Russian Academy of Sciences, prosp. 60-letiya Oktyabrya 7a, 117312 Moscow, Russia; e-mail: gorlova.da14@physics.msu.ru

1. Introduction

Modern experimental studies on the interaction of laser radiation with matter are mostly focused on the regime in which the intensity of this radiation exceeds the so-called relativistic intensity I (W cm^{-2}) $\approx a_0^2/\lambda_{\mathrm{las}}^2 \times 1.37 \times 10^{18}$, where λ_{las} (µm) is the wavelength of laser radiation; $a_0 = eA_0/(m_{\mathrm{e}}c)$ is the normalised vector potential; e is the electron charge; A_0 is the amplitude of the vector potential; m_{e} is the electron mass; and c is the speed of light. Nowadays, the maximum intensity achieved in the experiment is 5.5×10^{22} W cm^{-2} ($a_0 = 160$) [1], and real experiments are carried out in the intensity range $10^{18} - 10^{20}$ W cm^{-2} ($a_0 \sim 1-16$). In the near future, with the commissioning of new laser complexes within the framework of the ELI [2, 3] and other projects, a further increase in intensity up to 10^{23} W cm^{-2} is expected. Plasma formed during the interaction of such radiation with matter is an effective medium for accelerating electrons [4, 5], protons and heavy ions [6, 7], for obtaining directed beams of terahertz radiation [8, 9], X-rays and gamma radiation [10], as well as for designing secondary sources of neutrons [11, 12] and positrons [13, 14].

The key objective is to obtain directed electron beams with energies from units of MeV to units of GeV [15–17]. These beams can be used for developing laser-plasma sources of betatron radiation [18–20], for modelling astrophysical phenomena in the laboratory [21], for ultrafast electron microscopy [22], for designing sources of bremsstrahlung X-ray radiation [23], for nuclear spectroscopy [24], and for phase contrast radiography [25]. The most advanced laser-plasma sources of accelerated electron

beams have been fabricated in a gas with a low $(10^{17}-10^{19}$ cm$^{-3})$ density [26, 27]. At the same time, acceleration in a plasma with a near-critical density on the surface of a solid target provides a much higher beam charge, usually accompanied with a greater divergence and a wide quasi-exponential energy spectrum [28–30].

All mentioned works are based on the chirped-pulse amplification (CPA) technology [31] and its optical parametric chirped-pulse amplification (OPCPA) version [32]. Recently, an understanding has been gained that the temporal structure of a femtosecond pulse can have a vital influence on the physical processes occurring during laser-plasma interaction, especially in the regime of relativistic intensities and dense targets. This temporal structure can be quite complex and substantially depends on the features of the design of a particular laser facility [33–36]. Usually, part of the radiation that propagates in advance before the main pulse is characterised by the laser pulse contrast, which, however, can be different on different time scales – nano-, picosecond, and even subpicosecond. On the whole, the interaction of sufficiently intense radiation with the target before the arrival of the main pulse leads to the formation of a pre-plasma, which can both significantly degrade the characteristics of the generated beams of accelerated particles and X-ray photons, and contribute to a qualitative improvement of these characteristics, i.e., it makes it possible to control the laser-plasma interaction. In particular, this can be done by using additional laser pulses that form a pre-plasma with controlled parameters. Note that the presence of a pre-plasma must be taken into account when carrying out numerical simulations aimed at interpreting experimental results or at finding optimal interaction regimes.

This paper presents a review of the state-of-the-art research on the influence of the contrast of relativistically intense femtosecond laser radiation on its interaction with dense targets, on particle acceleration and generation of gamma radiation. In Section 2, the temporal structure of a femtosecond laser pulse is discussed in more detail, and the main components that must be taken into account (and measured) during research are identified. Section 3 is devoted to a general discussion of the effect of the contrast of a femtosecond laser pulse on the properties of the generated plasma and generation of the gamma radiation. Section 4 provides a review of works devoted to the formation of collimated beams of relativistic electrons from solid dense targets and the effect of contrast on this process. Section 5 deals with the role of contrast for ion acceleration. Finally, Section 6 discusses the interaction of radiation with structured targets, for which the role of contrast is even more important than for solid targets. In Conclusions, the main results of the research are presented.

2. Contrast of a femtosecond laser pulse

The temporal structure of a femtosecond laser pulse is rather complex and is determined by such basic elements (Fig. 1a) as a long nanosecond pedestal of amplified spontaneous emission (ASE), short femtosecond pulses travelling 5–100 ps ahead of the main pulse, and oscillations of the envelope at the pulse front.

Note that the use of a regenerative amplifier in the optical scheme of the laser will lead to the appearance of short pulses of significant amplitude, which are ~10 ns ahead of the main pulse and also significantly affect the processes of laser-plasma interaction [37, 38]. The characteristics of a long pre-pulse of spontaneous parametric emission in the OPCPA scheme [32] are also somewhat different.

There are a number of reasons for the appearance of pre-pulses. On a nanosecond time scale, they are the result of incomplete suppression of pulses preceding the main one in the master oscillator train by Pockels cells. On a picosecond scale, they are the result of scattering on lattices, uncompensated dispersion [39, 40], or nonlinear transformation [41–43] in the active element of the stretcher–amplifier–compressor system. Finally, there is a pedestal several nanoseconds long, associated with amplified spontaneous emission [44]. Accordingly, for the numerical characterisation of the temporal structure of the pulse, the concept of contrast K is introduced: the inverse ratio of the peak intensity of the main pulse to the
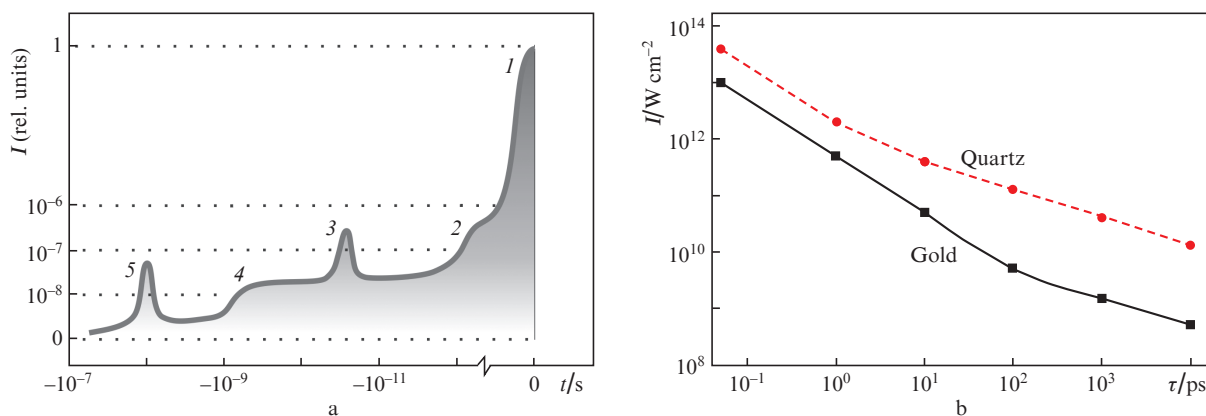
Figure 1. (a) Typical temporal structure of a laser pulse [(*1*) main pulse; (*2*) picosecond pedestal; (*3*) picosecond pre-pulse; (*4*) ASE pedestal; (*5*) nanosecond pre-pulse] and (b) the dependence of the intensity corresponding to the plasma formation threshold (data taken from [45]) for gold (metal) and quartz (dielectric) on the pulse duration.

intensity of one or another component of the temporal structure. In this regard, nanosecond and picosecond contrasts are distinguished, and the latter, as a rule, must be known on scales of both $10-100$ and $0.1-1$ ps.

For most solid targets, the plasma formation threshold at a nanosecond pulse duration is $10^9 - 10^{11}$ W cm^{-2} (Fig. 1b), while the typical ASE contrast, $K_{ASE} \sim 10^{-5} - 10^{-8}$ (if additional methods of contrast enhancement are not used) [33, 39], which causes the appearance of a pre-plasma when the intensity of the main pulse approaches 10^{18} W cm^{-2}. The formation of a pre-plasma under the action of ASE was experimentally discovered by Key et al. [46], and in modern experiments on the interaction of ultraintense laser radiation with matter, information about the parameters of the pre-plasma layer turns out to be critically important [47]. A plasma cloud can also be produced under the action of nanosecond and picosecond pre-pulses, the durations of which are comparable to the duration of the main pulse, and the intensities exceed $\sim 10^{13}$ W cm^{-2}.

Even for one particular laser system, contrast can vary dramatically. Figure 2a shows a typical third-order autocorrelation function of a femtosecond pulse for a terawatt laser system based on a Ti : sapphire crystal. The temporal profile of the pulse contains a pre-pulse at a delay $\Delta t_0 \sim -20$ ps (negative values of Δt_0 correspond to pre-pulses coming in advance of the main pulse) with a contrast $K_{ps} \sim 4 \times 10^{-5}$. Spikes at times -5.5 and -3 ps are artifacts ('ghosts') of the correlator and are caused by multiple reflections in nonlinear crystals. The ASE contrast K_{ASE} is $\sim 10^{-7}$ at $\Delta t_0 < -50$ ps. The contrast can be increased by using a scheme based on the generation of a cross-polarised wave (XPW) in the laser system [48]; the contrast is improved by a factor of about 100, up to $K_{ASE} \sim 10^{-9}$.

The ASE contrast can be controlled by varying the pump power of the master laser oscillator. Upon reaching a certain threshold for the pump power (which also depends on the alignment of the master oscillator), in addition to quasi-continuous femtosecond radiation, continuous-wave (cw) radiation appears [49]. Figures 2b and 2c show how the leading edge of the ASE (after the amplifiers) and the spectrum of the generated radiation (at the master oscillator output) change depending on the pump power of the master oscillator. The appearance of the cw component, despite the presence of a number of Pockels cells in the laser amplifier layout, leads to a deterioration in the K_{ASE} contrast from 10^{-7} to $\sim 10^{-5}$. The duration of such a pedestal is determined by the width of the time window of the Pockels cells and, in this case, is ~ 1.5 ns.

Contrast, as a quantity that determines the regime of interaction of a laser pulse with matter, is even more crucial in the case of using bulk or surface structured targets. The reason is that pre-ionisation, ablation, and even melting under the action of both short pre-pulses and ASE can change the shape of the structures, reduce their aspect ratio, or, in the case of 'poor' contrast, produce a pre-plasma layer with a significant density of electrons, which will not allow radiation to penetrate to dense structured layers of the target. In this case, the smaller the size of the structures used, the stronger the influence of these effects. If during preliminary ionisation and hydrodynamic expansion the characteristic scale of expansion of an individual structure becomes comparable to its size, then the main pulse will most likely interact with a quasi-uniform target. In addition, one should take into account the fact that structured samples have a reduced heat transfer into the target, which lowers the characteristic thresholds of ablation and melting in comparison with flat targets made of the same material. The strongest effect is exerted by ASE, which is difficult to suppress. It is the prolonged heating of the surface for hundreds of picoseconds/units of nanoseconds that most adversely affects the structures. Several times lower plasma formation threshold for structured targets was observed by Cristoforetti et al. [50].

The influence of pre-pulses on the properties of a plasma produced using structured targets is discussed in Refs [51, 52]. It is worth noting that Rajeev et al. [51] observed an opposite effect – an increase in the yield of X-ray radiation with an increase in the pre-pulse intensity. Work [52] belongs to the earliest studies of this direction. Little attention was paid to detailed contrast measurements at that time. More detailed studies of the melting thresholds for various kinds of nanostructures under the action of pulses emulating ASE were carried out in [53, 54]. It was shown that the local melting threshold strongly depends on the method of fabricating the structures. For example, samples obtained by deposition of germanium nanowires onto a substrate
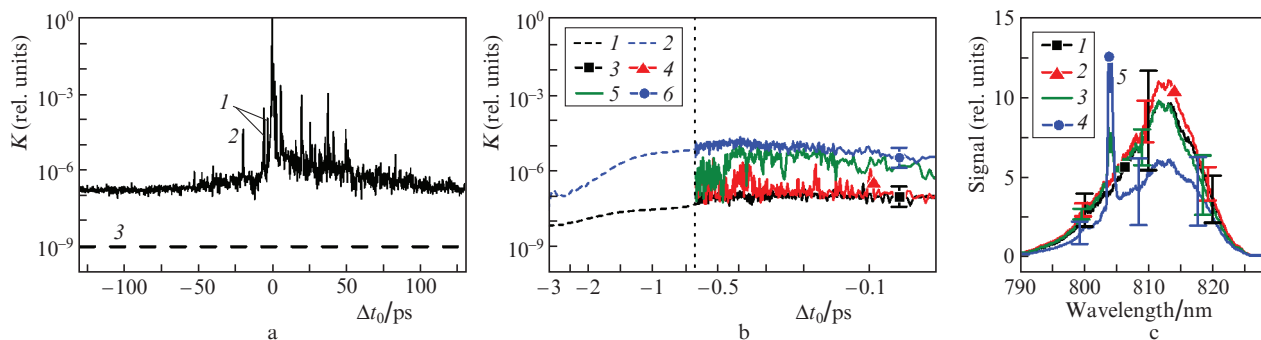
Figure 2. (Colour online) (a) Autocorrelation function of the 3rd order of a femtosecond pulse without using the XPW scheme (solid line, $K_{ASE} \sim 10^{-7}$): (*1*) artifacts of the correlator scheme; (*2*) pre-pulse with a delay $\Delta t_0 = -20$ ps; (*3*) ASE level using XPW (dashed line, $K_{ASE} \sim 10^{-9}$); (b) leading edges of pulses measured by a fast photodiode ($\Delta t_0 = -3 \ldots -0.6$ ns, dashed lines) at master oscillator pump powers of (*1*) 4.5 and (*2*) 5 W, as well as a third-order autocorrelator ($\Delta t_0 = -0.6 \ldots -0.05$ ns, solid lines) at pump powers of (*3*) 4.55, (*4*) 4.60, (*5*) 4.65, and (*6*) 4.70 W; (c) pulse spectra at pump powers of (*1*) 4.55, (*2*) 4.60, (*3*) 4.65 and (*4*) 4.70 W: peak (*5*) corresponds to cw radiation from the master laser oscillator.

(with relatively weak adhesion to the substrate itself) have an order of magnitude lower threshold (less than 0.03 J cm^{-2}) than a smooth surface made of the same material. This fact, of course, should be taken into account when carrying out laser-plasma experiments using high-intensity radiation.

Even a rough estimate of the characteristic parameters of the pre-plasma formed by pre-pulses of various nature is a complex experimental problem. In the literature, one can find only a small number of works in which simple estimates of the key plasma parameters (electron temperature, density, expansion velocity, etc.) are presented in a wide range of heating pulse parameters. Work [55] should be mentioned here. Nevertheless, the issues of the electron density profile and of the scale of the plasma expansion do not have a universal solution and still require the use of hydrodynamic calculations, as well as different experimental methods for direct and indirect estimates of the plasma state in each specific case.

The main parameter discussed in the literature is the length of the pre-plasma gradient L. We should dwell on it in detail, since this parameter is often used in works to characterise the regime of interaction of a laser pulse with a pre-plasma layer. It is customary to define the length of the pre-plasma layer as $L = |\mathrm{d}\ln n_e/\mathrm{d}x|_{x_0}^{-1}$; this quantity is usually compared with the wavelength of laser radiation: L/λ_0. By default, the derivative is taken at point x_0 [corresponding to the electron density $n_e(x_0) = n_0$], where laser radiation is absorbed (for example, $n_0 = n_{cr}$ at normal incidence of laser radiation, and n_{cr} is the critical electron density).

In the case of a short pre-plasma gradient ($L/\lambda_0 \leqslant 1$), information about the length of the pre-plasma layer indeed allows one to assume the dominant mechanism of electron acceleration. Thus, in the case of $L/\lambda_0 \ll 1$, vacuum heating manifests itself [56, 57], at a longer length ($0.1 < L/\lambda_0 \lesssim 1$) there occurs resonance absorption [58, 59] or $j \times B$ heating [5, 59, 60] (at $a_0 \geqslant 1$ and $L/\lambda_0 \sim 1$). In particular, the deviation of the direction of emission of hot electrons from the target from the normal to the direction of the radiation wave vector [61, 62] with increasing gradient length (or laser radiation intensity) is associated with the transition from resonant absorption to $j \times B$ heating.

With a further increase in the gradient length ($L/\lambda_0 > 1$), this parameter is still used, but it turns out to be insufficient, since in this case the processes associated with the propagation of a laser pulse in a plasma began to occur, the efficiency of which largely depends on the distribution and value of the electron density n_e. They include parametric processes [63], ponderomotive and relativistic self-focusing [5, 59], as well as ionisation defocusing [5] of a laser beam, etc.

The parameters of the electron density profile are determined using experimental methods and/or numerical simulation. The simplest experimental method is shadow photography [62, 64–68]. Based on the size of the plasma shadow and on the assumption of the exponential shape of the low-density tail of the electron profile, one can estimate the length of the pre-plasma gradient in this region [62, 64–66]. This method also makes it possible to track changes in the shape of the pre-plasma cloud [69, 70], in particular, the appearance of plasma channels in it [67, 71]. Interferometry can be used for the same purposes [64, 68, 71–74], which makes it possible to reconstruct the

electron density profile (up to the boundary of the shadow from the plasma cloud). The disadvantage of interferometry is the ambiguity of reconstructing the electron profile, for example, due to the assumption of its axial symmetry, which is not always true. A common disadvantage of these two methods is the impossibility of probing dense plasma regions ($n_e \sim n_{cr}$), in which laser radiation energy is absorbed or plasma waves are excited (at $n_e \sim n_{cr}/4$ [63]), without using X-ray sources [75]. Ivanov et al. [68] proposed to estimate the length of the pre-plasma layer in the region of high [$n_e \sim (0.25–0.5)n_{cr}$] electron density by comparing the experimentally measured spectra of optical plasma radiation (second and three-half harmonics of the fundamental radiation) with the spectra obtained from numerical particle-in-cell (PIC) simulation.

Usually, to determine the parameters of the pre-plasma gradient in a dense plasma, the experimental data obtained by interferometry or shadow photography are supplemented by the results of numerical 1D [28, 64, 67, 76–78] or 2D [70, 72, 79] hydrodynamic modelling. It should be noted that 1D modelling does not allow two-dimensional distortions of the pre-plasma gradient to be modelled [70], and can also unreliably describe the process of plasma expansion [80, 81], and therefore should be used only for preliminary estimates.

3. Plasma formation and the role of contrast at relativistic laser radiation intensities

The most obvious diagnostics of the processes occurring during the interaction of high-power laser radiation with plasma is the measurement of the absorption coefficient of the incident radiation from the reflected laser beam. At the same time, in the case of relativistic intensities, reflection from the plasma is not specular (there is a strong distortion of the laser beam in the plasma due to self-action and other nonlinear processes, as well as a significant diffuse component).

Singh et al. [82] measured the absorption coefficients of the laser radiation energy during the interaction of a laser pulse ($\tau = 30$ fs, $\lambda = 800$ nm, incidence angle of $\theta = 40°$) with a thick aluminium target for a wide range of intensities ($10^{17}–10^{18}$ W cm^{-2}) and K_{ASE} contrasts (10^{-5}, 10^{-7}, and 10^{-9}). The observed increase in the absorption coefficient with an improvement in contrast indicated an increase in the efficiency of conversion of the laser radiation energy into the kinetic energy of electrons. The highest absorption coefficient was observed at a contrast of 10^{-9}: It was 60%–70% and 50%–60% for p- and s-polarised laser radiation, respectively. At a contrast of 10^{-5}, the absorption coefficient was 10% lower. The smallest absorption coefficient was observed at $K_{ASE} \sim 10^{-7}$: 45%–55% and 20%–35% for p- and s-polarised laser radiation, respectively. With the best contrast, Singh et al. [82] considered ponderomotive acceleration at a sharp plasma–vacuum interface as a radiation absorption mechanism; there was no discussion of the acceleration mechanisms with the deterioration of contrast in this work.

Far more informative diagnostics of the processes occurring during the interaction of high-power laser radiation with plasma are the diagnostics of plasma bremsstrahlung radiation, as well as direct measurement of the characteristics of electron fluxes from the plasma. Indeed,

the spectra of X-ray and gamma radiation carry information about the hot electrons formed in the plasma, their energy and angular spectra and, consequently, about the mechanisms of the appearance of such electrons, about the absorption of laser radiation energy in a dense plasma, etc. The first experimental works devoted to the influence of contrast on the energy and yield of characteristic X-ray radiation appeared in the 1990s [83–85]. In further studies, both the positive and negative effects of pre-pulses and the pre-plasma generated by them were considered using various experimental schemes.

In [86, 87], the interaction of a laser pulse ($\tau = 50$ fs, $\lambda = 800$ nm, $I \sim 10^{18}$ W cm^{-2}, p polarisation, $K_{ASE} \sim 10^{-5}$, and $\theta = 45°$) with thick molybdenum plates was experimentally investigated. By switching off and misaligning the Pockels cells in the laser system, the contrast determined by the amplitude of a short pre-pulse 13 ns ahead of the main pulse was varied from 2.5×10^{-7} to 10^{-2}. It was shown that the deterioration of the contrast K_{ns} to less than 2×10^{-3} leads to a sharp (more than twofold) increase in the 'temperature' of the bremsstrahlung X-ray radiation from $\sim 134 \pm 9$ to ~ 300 keV (hereafter, we mean the exponent at exponential approximation of emission spectra or electrons). Note that in this case, ASE played a significant role in the formation of the pre-plasma gradient, since its intensity significantly exceeded the plasma formation threshold.

The results of comparative studies of the generation of bremsstrahlung gamma radiation under three different measurement regimes (Table 1) were presented in works [37].

Table 1. Contrast of laser radiation in different measurement regimes [37].

Regime	K_{ASE}	Picosecond pre-pulse		Nanosecond pre-pulse	
		Delay/ps	K_{ps}	Delay/ns	K_{ns}
1	10^{-5}	25	5×10^{-3}	12.5	2×10^{-6}
2	10^{-8}	12	6×10^{-7}	12.5	5×10^{-8}
3	10^{-8}	12	6×10^{-7}	12.5	3×10^{-4}

In these experiments, a laser pulse ($\tau = 45$ fs, $\lambda = 800$ nm, $I \sim 10^{18}$ W cm^{-2}, p polarisation, and $\theta = 45°$) was focused on thick plates of steel and lead. Bremsstrahlung gamma radiation was recorded by a scintillation detector based on a NaI crystal [88]. In regime 2, the gamma radiation temperature of 65 ± 10 and 180 ± 20 keV on a steel target at $I \sim 7 \times 10^{17}$ and 2×10^{18} W cm^{-2}, respectively, correlated with the estimates for resonant absorption [89] and ponderomotive acceleration [90] (that is, in this regime, the main pulse interacted with a sharp pre-plasma layer, $L/\lambda \ll 1$). At a high ASE level (regime 1), a long ($L/\lambda > 100$) and dense pre-plasma layer forms on the target surface, which leads to an increase in temperature to 115 ± 10 keV on a steel target at $I \sim 7 \times 10^{17}$ W cm^{-2} and to 370 ± 120 keV on a lead target at $I \sim 10^{18}$ W cm^{-2}. A significant increase in temperature on a lead target is associated with a lower threshold for plasma formation [69]. The introduction of a nanosecond pre-pulse into the temporal structure at high K_{ASE} (regime 3), on the contrary, leads to a decrease in the gamma radiation temperature T_h to 135 ± 10 keV on a steel target at $I \sim 2 \times 10^{18}$ W cm^{-2}. In this case, a long but rarefied pre-plasma layer forms on

the target surface, which leads to a decrease in the laser radiation intensity in the region of efficient generation of fast electrons. With poor K_{ASE} (regime 1), the effect of an additional increase in the gamma radiation temperature observed with an increase in the duration of the laser pulse from 45 to 350 fs with the conservation of its energy (that is, with a decrease in intensity). The temperature of gamma radiation increased to 640 ± 115 keV on a lead target at $I \sim 10^{17}$ W cm^{-2}.

It was experimentally shown in [91, 92] that the yield of characteristic X-ray radiation generated by irradiating thin (300 nm and 20 µm) Cu and Ti targets with a laser pulse ($\tau = 150$ fs, $\lambda = 800$ nm, $I \sim 10^{17}$ W cm^{-2}, p polarisation, $K_{ASE} \sim 10^{-8}$, and $\theta = 25–55°$) can be optimised by varying the delay ($\Delta t_0 = -5 \ldots -25$ ps) between the main pulse and a short artificial pre-pulse ($\tau = 150$ fs, $I \sim 10^{14}$ W cm^{-2}). Numerical PIC simulation has shown that this effect is associated with the optimisation of the absorption coefficient of laser radiation with a change in the length of the pre-plasma layer ($L/\lambda \sim 0.01–1$).

In work [77], an electron beam was observed that was generated along the normal to the front surface of a thick copper target irradiated by a laser pulse ($\lambda = 800$ nm, $K_{ASE} \sim 10^{-6}$, and $\theta = 45°$) at various intensities [$I \sim (0.4–4) \times 10^{17}$ W cm^{-2} at $\tau = 45$ fs], durations ($\tau = 45–1200$ fs at a fluence of $\sim 2 \times 10^4$ J cm^{-2}) and polarisations. The appearance of the beam was attributed by the authors to the formation of a pre-plasma layer on the target surface due to ASE. The beam was observed accross the entire range of the varied parameters and had a divergence of $\sim 20°$. The electron temperature depended on the intensity as $\propto I^{2/3}$ and was 290 and 160 keV at $I \sim 4 \times 10^{17}$ W cm^{-2} for p and s polarisations, respectively, which exceeds the estimate (the so-called Beg's law [89]) $T_h \approx 215 (I_{18} \lambda_{\mu m}^2)^{1/3}$ (keV) (here I_{18} is the intensity of the incident radiation, normalised to 10^{18} W cm^{-2}, and $\lambda_{\mu m}$ is the wavelength of the light wave in µm), which is usually associated with the effect of resonant absorption. With an increase in the laser pulse duration, the electron temperature decreased, which contradicts the results of [37], where the ASE contrast was an order of magnitude worse ($\sim 10^{-5}$).

Thus, the ASE contrast plays the main role in the formation of a pre-plasma, which facilitates the absorption of laser radiation and the acceleration of electrons to energies significantly exceeding the ponderomotive energy upon focusing into vacuum, while short pre-pulses are not so important (if their amplitude is sufficiently small). Therefore, to produce a pre-plasma, it is better to use an artificial nanosecond pre-pulse, the parameters of which (energy, wavelength, and beam diameter) can be easily controlled independently of the parameters of the main femtosecond pulse. In this case, the latter, generally speaking, should have good contrast values for all pre-pulses and ASE.

Jarrott et al. [76] investigated the yield of the characteristic (K_α) and bremsstrahlung radiation generated by the interaction of a laser pulse ($\tau = 40$ ps, $\lambda = 1050$ nm, $\varepsilon \sim 300$ J, $I \sim 8 \times 10^{17}$ W cm^{-2}, and $\theta = 16°$) with a 12-µm-thick silver foil as a function of the contrast ($K_{ns} \sim 10^{-6}$, 10^{-5}, or 10^{-4}) determined by a long artificial pre-pulse ($\tau = 3$ ns, $\lambda = 1053$ nm). The pre-pulse was 3 ns ahead of the main pulse. As the contrast deteriorated from 10^{-6} to 10^{-4}, the yield of K_α radiation decreased from $(10 \pm 2) \times 10^{11}$ to $(3 \pm$

0.6) $\times 10^{11}$ quantum sr^{-1}, as well as the yield of bremsstrahlung with an energy of less than 1 MeV. On the other hand, the yield of electrons (with an energy of $0-5$ MeV), recorded by an electron spectrometer from the rear surface of the target, increased from 1×10^{12} to 5×10^{12} pcs MeV^{-1} sr^{-1}, and the total energy removal by electrons increased from 0.6 to 1.8 J. Therefore, Jarrott et al. [76] associated the decrease in the X-ray radiation yield with an increase in the conversion of laser radiation energy into the kinetic energy of electrons and with a decrease in the number of repeated passes through the target material of electrons returned by the ambipolar field of ions.

Santala et al. [62] investigated the directivity of a bremsstrahlung gamma-ray beam during the interaction of a laser pulse [$\tau = 1-1.5$ ps, $\lambda = 1054$ nm, $\varepsilon \sim 20-50$ J, $I \sim (1-3) \times 10^{19}$ W cm^{-2}, p polarisation, and $\theta = 45°$) with a thick composite target made of tantalum (1.75 mm thick) and copper (3 mm thick). To produce a relatively short pre-plasma ($L/\lambda = 2.6-5.9$), the duration of the ASE pedestal was varied from 0.3 to 1 ns (the K_{ASE} value is not indicated), and an artificial pre-pulse (6% of the main pulse energy) arriving $0.3-1.5$ ns before the main pulse was used to generate a long pre-plasma layer. Gamma radiation was recorded using the activation reaction $^{63}Cu(\gamma, n)^{62}Cu$ (reaction threshold 10 MeV) in copper blocks located around the target. At $L/\lambda \sim 1$, an increase in the pre-plasma length led to a shift in the predominant direction of generation of gamma radiation from the normal to the rear surface of the target (which corresponds to resonance absorption) to the direction along the wave vector (which corresponds to $j \times B$ heating). The angular beam width was $35-40°$, and the temperature was $1-4$ MeV. At large lengths of the pre-plasma layer ($L/\lambda \sim 100$), the direction of generation of gamma radiation became chaotic, changing from shot to shot.

Courtois et al. [64] characterised the source of bremsstrahlung gamma radiation in an experimental scheme close to that described in the previous paragraph. Laser radiation ($\tau = 1$ ps, $\lambda = 1053$ nm, $\varepsilon \sim 30$ J, $I \sim 10^{19}$ W cm^{-2}, p polarisation, and $\theta = 45°$) was focused on a thick composite target made of plastic (10 μm thick) and tantalum (2 mm thick). The pre-plasma was formed by an artificial pre-pulse ($\tau = 450$ ps, $\varepsilon \sim 15$ J, $I \sim 10^{14}$ W cm^{-2}, and $K_{ps} \sim 10^{-5}$), and its length L was varied from 20 to 60 μm by changing the delay between pulses. The angular distribution and energy spectrum of gamma quanta (in the energy range exceeding 10 MeV) were measured by the activation method in the reactions $^{63}Cu(\gamma, n)^{62}Cu$ (10 MeV threshold) and $^{12}C(\gamma, n)^{11}C$ (19 MeV threshold) in blocks located around the target; dose and distribution of X-ray radiation (over 200 keV) were measured by silicon diodes. The structure and size of the radiation source were reconstructed by analysing the penumbra of a thick lead diaphragm. The gamma-ray beam was generated along the normal to the rear side of the target. With an increase in the length of the pre-plasma, the beam expanded (from 20 to 40°), and there was observed an increase in the temperature (from ~1.5 to 2.7 MeV), the flux (from 1 to 2.7 $\times 10^9$ quanta sr^{-1}) of gamma quanta, and the dose (from ~5 to 12 mrad per 1 m of air) of X-ray radiation. A threefold decrease in the intensity of the main pulse did not affect the distribution of gamma quanta and the temperature of the source, but proportionally reduced the flux of gamma quanta and the dose of X-ray radiation. The size of the gamma-ray source was ~200 μm. Hot spots existing at $L \sim$

$20-40$ μm disappeared when the pre-plasma was lengthened, and the source structure became more symmetric and stable. Numerical PIC simulation showed that the variability of the source structure and the appearance of hot spots in it at $L \sim 40$ μm are explained by the decay of the laser beam in the pre-plasma into separate filaments.

Malka et al. [67] determined the interaction regime not only by the pre-plasma parameters, but also by the intensity of the main pulse ($\tau = 300-500$ fs, $\lambda = 1058$ nm, $\varepsilon \sim 15$ J, $I \sim 10^{19}$ W cm^{-2}, $K_{ASE} < 2 \times 10^{-8}$ at delays of more than 50 ps, and $\theta = 0$). A thin (0.3 μm) plastic target was used. The pre-plasma was produced by a counter-propagating laser pulse ($\tau = 750$ ps, $\lambda = 1058$ nm, $I \sim (3-5) \times 10^{12}$ W cm^{-2}, and $\theta = 35°$) focused on the film surface from its rear side. The delay between pulses was $500-850$ ps. The electron density n_e in the pre-plasma layer was $(0.1-0.2)n_{cr}$. At a radiation intensity of ~4 $\times 10^{18}$ W cm^{-2}, the temperature of electrons escaping from the rear side of the target was ~1 MeV. At an intensity of more than 5×10^{18} W cm^{-2}, the plasma transmission increased from 5% to 20%–30%. A new electronic component with a temperature of ~3 MeV and a maximum electron energy of up to 20 MeV appeared in the electronic spectrum. Shadowgraphy measurements and modelling of the propagation of a radiation pulse with an intensity of ~6 $\times 10^{18}$ W cm^{-2} in the pre-plasma showed the presence of self-focusing, leading to the formation of a plasma channel. The radiation intensity in the channel reached ~10^{20} W cm^{-2}. The appearance of a new electronic component is explained by the direct acceleration of electrons in the channel under the action of the Lorentz force ($j \times B$) by a laser pulse with an increased intensity.

Gizzi et al. [71] introduced two artificial pre-pulses into the temporal structure of the pulse ($\tau = 1$ ps, $\lambda = 1054$ nm, $\varepsilon \sim 50$ J, $I \sim 5 \times 10^{19}$ W cm^{-2}, and $\theta = 0$). The first one ($\tau = 600$ ps, $\lambda = 527$ nm, $I \sim 5 \times 10^{14}$ W cm^{-2}, and $K_{ns} \sim 10^{-5}$) preceeded the main pulse by 1.3 ns and produced a pre-plasma layer with $n_e \sim 0.1 n_{cr}$. The second one ($\tau = 1$ ps, and $\lambda = 1054$ nm) was used to form a channel in the pre-plasma layer. The time it was ahead of the main pulse varied from 20 to 120 ps. Plastic films 0.1, 0.3, and 0.5 μm thick were used as targets. The channel parameters were monitored using interferometry; plasma bremsstrahlung radiation was recorded by scintillation detectors. It was shown that the integral energy of gamma quanta increases fourfold when the delay between the main pulse and the short, channel-producing, pre-pulse increased from 20 to 120 ps (for a target thickness of 0.3 μm). Also, in this case, the plasma transmission increases threefold, from 13% to 38%, and the regime of gamma radiation generation in the presence of the channel becomes more stable.

Thus, the appearance of relativistic electrons during the propagation of a laser pulse with an intensity of $10^{19}-10^{20}$ W cm^{-2} in an extended pre-plasma layer with a density much lower than the critical one is associated with self-focusing of radiation with the subsequent formation of a channel in the plasma [72]. However, an increase in the radiation intensity or the electron density of the pre-plasma layer in the region of the laser beam waist leads to the splitting of this beam into separate filaments and to a decrease in the efficiency of electron acceleration. In addition, the reaching of plasma regions with a near-critical electron density (near the target surface) by the laser beam also leads to

effective heating and acceleration of electrons. At lower intensities, plasma waves play a crucial role. In [37], using the 3D3V PIC code Mandor [93], a numerical PIC simulation of the propagation of a laser pulse (τ = 50 fs, I = 10^{18} W cm^{-2}) was performed at various lengths L of the density gradient n_e. In the case of a long ($L/\lambda \sim 100$) gradient (density n_e linearly increasing to $0.4n_{cr}$), the generation of high-energy electrons is caused by self-focusing of radiation at $n_e < 0.2n_{cr}$, as well as the excitation and breaking of plasma waves at $n_e \sim (0.3-0.4)n_{cr}$.

The results of a more systematic study of the effect of the pre-pulse were published in [68, 74, 94–96], where a nanosecond Nd:YAG laser pulse was used as a pre-pulse (τ = 6.8 ns; λ = 532, 1064 nm; and $I \sim 10^{12}$ W cm^{-2}). The delay between nanosecond and femtosecond (τ = 50 ± 5 fs, λ = 813 nm, $I \sim 2 \times 10^{18}$ W cm^{-2}, p polarisation, $K_{ASE} \sim 10^{-6}-10^{-9}$, and $\theta = 45°$) pulses determined the shape of the pre-plasma gradient. Thick molybdenum and tungsten targets were used.

A typical dependence of the integral yield of gamma radiation (map) on the delay Δt_0 between femtosecond (FS) and nanosecond (NS) pulses and the position of the focal plane relative to the initial target surface (focusing depth f_0) is shown in Fig. 3a. The delay Δt_0 could be set from +5 to –40 ns (with negative delays, the NS pulse was ahead of the FS pulse). A significant increase in the temperature T_h and the yield of gamma radiation in comparison with the case of a single FS pulse was observed at Δt_0 = +5...–10 ns (first maximum) and Δt_0 = –20...–40 ns (second maximum). (For a single FS pulse, $T_h \sim 150 \pm 15$ keV, and the maximum energy of gamma radiation is ~ 1.5 MeV.) In the range Δt_0 = –10...–20 ns, the output of gamma radiation dropped to zero. In the region of delays corresponding to the second maximum, an increased yield

of gamma radiation was observed when the FS pulse was focused over the target surface: $f_0 = -50...-100$ μm. In the region of the first maximum, an increase in the temperature of gamma radiation to $\sim 1.6 \pm 0.3$ MeV (by a factor of 10) and the maximum energy to ~ 7.5 MeV (by a factor of 7) was recorded [68].

The contrast K_{ASE} significantly affects the output of gamma radiation at delays corresponding to the second maximum (Fig. 3b) [96]. It was shown that when the contrast increases to $K_{ASE} < 10^{-9}$, the second maximum disappears. An increased yield of gamma radiation at delays corresponding to the second maximum appears at $K_{ASE} \sim 10^{-7}$. With a further decrease in contrast to $K_{ASE} \sim 10^{-5}$, the yield of gamma radiation increases, while the optimal focusing depth f_0 corresponds to a point above the target surface. The appearance of the second maximum is most likely associated with the formation of a short pre-plasma gradient upon heating of a strongly scattered cold recombining plasma under the action of the ASE of the main FS pulse.

An increase in the yield of gamma radiation was correlated with the appearance of three-half harmonic of an FS pulse in plasma optical radiation spectrum. Diagnostics of optical plasma radiation and the results of PIC simulation by the Mandor code showed [68] that at small delays between pulses (the first maximum) in the range $n_e \sim (0.25-1)n_{cr}$, a relatively short pre-plasma gradient is produced, $L/\lambda \sim 1-2$. This favours the efficient excitation of parametric instabilities (Raman scattering, two-plasmon decay). The electrons, which received energy as a result of the breaking of plasma waves, are accelerated in the field of the FS laser pulse (if they are injected in the correct phase), which explains the generation of fast electrons, includ-
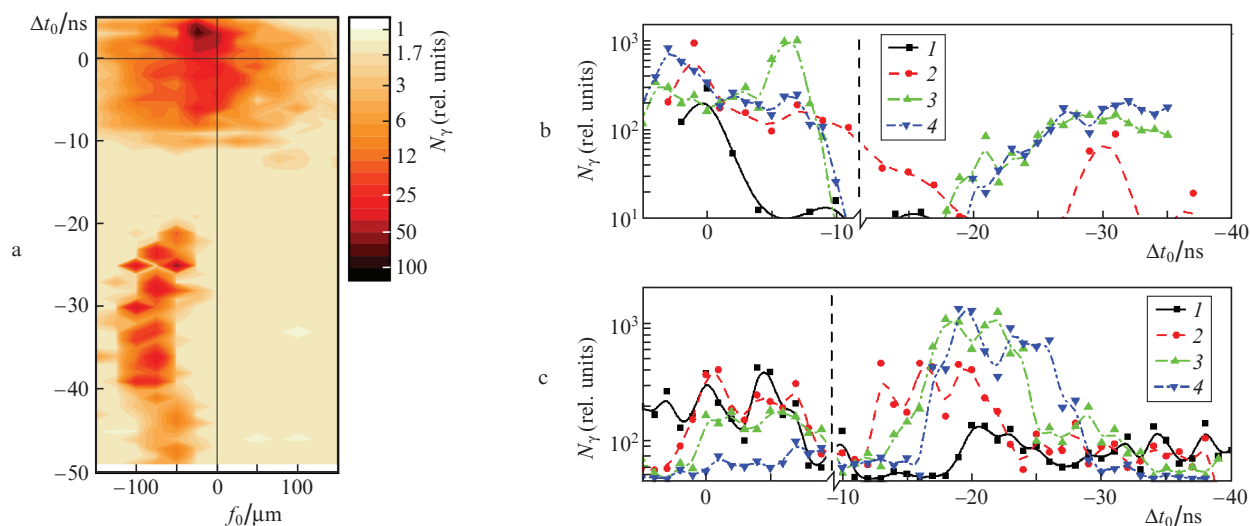
Figure 3. (Colour online) (a) Typical dependence of the integral yield of gamma radiation of N_γ plasma on the delay Δt_0 between FS and NS pulses and the position of the focal plane relative to the initial target surface (focusing depth f_0) at τ = 50 ± 5 fs, $K_{ASE} \sim 10^{-7}-10^{-6}$, Mo 2-mm-thick target [68]; (b) map cross sections at τ = 50 fs and (*1*) $K_{ASE} < 10^{-9}$, $f_0 = -25$ μm; (*2*) $K_{ASE} \sim 10^{-7}$, $f_0 = -25$ μm; (*3*) $K_{ASE} \sim 10^{-5}$, $f_0 = -25$ μm at $\Delta t_0 > -12$ ns and $f_0 = -100$ μm at $\Delta t_0 \leqslant -12$ ns; (*4*) $K_{ASE} > 10^{-5}$, $f_0 = -25$ μm at $\Delta t_0 > -12$ ns and $f_0 = -90$ μm at $\Delta t_0 \leqslant -12$ ns [96]; and (c) map cross sections at a constant FS pulse energy, $K_{ASE} \sim 10^{-7}$ and (*1*) τ = 50 fs, $I = 3 \times 10^{18}$ W cm^{-2}, $f_0 = -10$ μm; (*2*) τ = 570 fs, $I = 2 \times 10^{17}$ W cm^{-2}, $f_0 = -10$ μm at $\Delta t_0 > -10$ ns and $f_0 = -75$ μm at $\Delta t_0 \leqslant -10$ ns; (*3*) τ = 1130 fs, $I = 1 \times 10^{17}$ W cm^{-2}, $f_0 = -10$ μm at $\Delta t_0 > -10$ ns and $f_0 = -105$ μm at $\Delta t_0 \leqslant -10$ ns; (*4*) τ = 1700 ± 100 fs, $I = 8 \times 10^{16}$ W cm^{-2}, $f_0 = -10$ μm at $\Delta t_0 > -10$ ns and $f_0 = -140$ μm at $\Delta t_0 \leqslant -10$ ns [74]. In calculating the cross sections for each delay, the average value of the yield N_γ over the focusing depth f_0 in the region of ±25 μm is presented.

ing in the form of a beam (see Section 4 for more details).

The expansion of the plasma after the end of the NS pulse leads to the formation of a sufficiently extended plasma with $L/\lambda \sim 10-100$, which causes a sharp drop in the gamma radiation yield. The most probable reasons for this are the distortion and ionisation defocusing of the FS beam, which is partially confirmed by the numerical simulation of the propagation of the FS pulse in the pre-plasma, taking into account field ionisation, based on the results of interferometry [73].

To reduce the negative role of ionisation, a polyethylene film $200-400$ μm thick was placed on the front surface of the target in a number of experiments [97]. This made it possible to increase the temperature of gamma radiation at the second maximum (with an NS radiation pulse at $\lambda = 1064$ nm) and the maximum energy to ~ 2 MeV and to 10 MeV, respectively, and initiate the photodisintegration of deuterium $D(\gamma, n)H$ (2.23 MeV threshold) with a yield of 8 ± 1 neutrons per pulse (in 4π) [98].

However, ionisation can also play a positive role. An increase in the FS pulse duration from 50 to 1700 fs at constant energy (the intensity decreases from 3×10^{18} to 8×10^{16} W cm^{-2}) leads to an increase in the integral gamma radiation yield at the second maximum by more than 10 times compared to the initial level, by $2-3$ times compared to the yield in the first maximum at the minimum duration, and by 30 times compared to the yield in the case of a single FS pulse without an NS pre-pulse ([74], Fig. 3c). Using the interferometry data, as well as diagnostics of optical and gamma radiation of plasma in the regime of a long FS pulse, it was revealed that collisional ionisation of atoms by electrons oscillating in the field of such a pulse plays a significant role in the formation of the electron density profile at delays corresponding to the second maximum of the gamma radiation yield. Numerical simulations have shown that the acceleration of electrons in this case is caused by the breaking of plasma waves excited by stimulated Raman scattering of laser radiation in a plasma with $n_e = 0.25n_{cr}$.

4. Formation of beams of relativistic electrons

The idea of accelerating electrons by high-power laser pulses has been existing for over 40 years. In 1979, Dawson and Tajima [99] proposed the concept of a 'laser accelerator', in which a laser pulse propagating in a rarefied subcritical plasma excites a plasma wave that accelerates electrons to high energies (up to GeV and higher). Later, this mechanism became known as laser wakefield acceleration (LWFA) and was investigated in many works (see, for example, [15, 100-102]).

There are much fewer works devoted to the study of electron acceleration using solid targets, which is due to the fact that the electrons produced in such an interaction have lower energies (units to hundreds of MeV), a wide, most often quasi-exponential, spectrum and a large divergence (up to $1-10$ sr), that is, their parameters are worse than those obtained using accelerators. However, the use of solid targets has its own advantages: a higher charge of the generated beams, the possibility of accelerating ions along with

electrons, and the accompanying generation of X-rays and gamma rays.

It is worth noting that there are a number of theoretical works which predicted the formation of electron beams with a high charge (up to nC) in LWFA. For example, based on the result of 1D and 2D PIC simulations, Li et al. [103] demonstrated the possibility of forming an electron beam with a charge of ~ 1 nC using a gas jet with a specially formed inhomogeneous profile. Such large charges are obtained due to the effective self-injection of electrons into the wake wave [104], with the diffused plasma–vacuum interface actually leading to an improvement in the beam parameters [105]. However, the ideas proposed in these works have not yet been experimentally confirmed (due to the complexity of forming the required electron density profile or the absence of laser systems with the required parameters). At the moment, the experimentally achieved beam charges using LWFA in a gas jet are still significantly lower than the charges obtained using solid targets (hundreds of pC [106] vs. ~ 100 nC [107]).

A large number of studies examining the acceleration of electrons to relativistic energies in the interaction of ultraintense laser radiation with solid targets took place in the 1990s. One of the first papers on this topic is the work of P. Gibbon [108]. In particular, using PIC modelling, he found that electrons are accelerated to energies of several MeV when a p-polarised Gaussian laser pulse with an intensity $I \sim 10^{18}$ W cm^{-2} interacts with a supercritical plasma ($n_e/n_{cr} = 2-10$) having an ideally sharp boundary (the profile looked like a step). Such studies were motivated, in particular, by the problems of controlled thermonuclear fusion.

A typical energy spectrum of electrons in this regime can be described by an exponential dependence with an exponent ('temperature') $T_h \approx 0.5a_0^{4/3}$ [89]. Based on the analysis of various models and numerical calculations, Compant La Fontaine [109] obtained a different estimate, relying on the laws of conservation of energy and momentum: $T_h \approx 0.35a_0\sqrt{\eta_e}$, where $\eta_e \approx (5 \times 10^{-2})a_0^{3/2}$ is the fraction energy transferred to fast plasma electrons [46]. In addition, the dependence of the 'temperature' of the generated electrons on the target material was found [110]. The angular spectrum of electrons during such acceleration is wide, with a divergence of up to several radians, which complicates the practical use of the source.

In a recent paper [111], it was shown that the mechanisms of wakefield acceleration can be realised not only in gases, but also with the use of solid targets. The regime of electron generation using laser pulses with a sufficiently low energy and short duration ($\varepsilon = 2.6$ mJ, $\tau = 3.5-24$ fs, and $K_{ps} = 10^{-10}$) and a SiO_2 target was considered. Part (4% in energy) of the main pulse was used to produce a homogeneous pre-plasma. The pre-plasma gradient length L/λ was varied from ~ 0.2 to several units by changing the delay ($0-300$ ps). It was shown that for the case $L \sim \lambda$ at such parameters, the manifestation of LWFA is possible, since a short (3.5 fs) pulse can resonantly excite waves in a plasma with an electron density of the order of the critical one, which is not observed for a longer pulse (24 fs). In this case, the main source of injection is electrons from the L-shell of the silicon atom.

Gahn et al. [112] also proposed to use high-pressure gas jets as a target, which, upon ionisation, are capable of generating a plasma with a concentration close to the critical one [$(0.1-0.5)n_{cr}$]. It was shown that at a certain plasma concentration, the effect of self-channelling of radiation is possible (for example, at $\tau = 200$ fs, $\varepsilon = 250$ mJ, and $I \sim 4 \times 10^{18}$ W cm^{-2}, the channel length reaches hundreds of microns) and electrons are accelerated in the formed channel to energies of ~ 1 MeV. This mechanism is called direct laser acceleration (DLA) and is also observed upon oblique incidence of high intense laser radiation on subcritical plasma, the concentration profile of which must satisfy certain requirements (see below) [107, 113].

In the last decade, there has been a renewed surge of interest in the acceleration of electrons using solid targets. It is associated both with the development of laser technology (the appearance of petawatt laser systems, the achievement of relativistic intensities at a pulse repetition rate of $1-10$ kHz [114]) and with the peculiarities of the parameters of the generated electron beams (first of all, with the possibility of obtaining a large charge, as well as with the development of methods that ensure the collimation of the resulting beam). For example, Mordovanakis et al. [28] obtained stable electron beams with an energy of up to 2 MeV and a charge of 7 pC during the interaction of laser pulses ($\tau = 30$ fs, $\lambda = 800$ nm, $\varepsilon \sim 3$ mJ, $I \sim 2 \times 10^{18}$ W cm^{-2}, $K_{ASE} \sim 4.5 \times 10^{-11}$, and $\theta = 45°$) having a repetition rate of 0.5 kHz with a SiO$_2$ target in the presence of an artificial pre-pulse ($\tau \sim 30$ fs, $I \sim 2 \times 10^{14}$ W cm^{-2}, and $K_{fs} \sim 10^{-4}$). The delay between pulses was varied from 0 to 187 ps, while the length of the pre-plasma layer L, according to the authors' estimates, varied from less than 0.1 to 5.5λ. When the delay was varied from 0 to 16.7 ps, the electron beam was generated at an angle of 36° from the normal to the target surface, and its charge increased, reaching a maximum at $L/\lambda = 0.5$.

Electron beams can be generated even at subrelativistic laser radiation intensities. For example, Li et al. [40] obtained a quasi-monoenergetic beam ($E \sim 100$ keV, $Q = 9$ pC) generated by the interaction of a laser beam ($\tau = 65$ fs, $I \sim 10^{17}$ W cm^{-2}, $K_{ps} \sim 10^{-7}$) with a target made of aluminium. The characteristic scale of the pre-plasma gradient L was $0.1-0.5\lambda$. The generation of an electron beam is described using a two-stage model: First, a plasma wave is excited by laser radiation in a subcritical plasma, from which at certain times part of the electrons is 'ejected' in the direction of the reflected radiation. The moment of ejection of the electron beam is determined by the dynamics of the interference pattern formed by the incident and reflected beams. Then these electrons are deflected towards the normal under the action of the ponderomotive field of the interference pattern. This model was confirmed in PIC simulations, which were carried out for $L/\lambda = 0.2$; no further study of the effect of pre-plasma parameters on electron acceleration was performed.

Quasi-monoenergetic electron beams with energies of $0.2-0.8$ MeV and a divergence of ~ 0.1 rad were also obtained in [115] by the interaction of laser radiation ($\tau = 60$ fs, $I \sim 2 \times 10^{17}$ W cm^{-2}) with the edge of a 200-μm-thick aluminium foil. Since the laser radiation contained a high-power pre-pulse ($K_{ns} \sim 10^{-4}$), the main radiation interacted with the pre-plasma gradient, and its characteristic scale was estimated as $L/\lambda \sim 15$. The PIC simulation showed

that electrons are accelerated in a plasma wave that is generated as a result of self-modulation instability of an intense laser pulse during its propagation in an inhomogeneous pre-plasma. Wang et al. [116] studied the angular and energy distributions of electrons for the case of laser pulses with intensities of $10^{16}-10^{18}$ W cm^{-2} ($K_{ps} \sim 10^{-7}$). The target was a 5-mm-thick Al plate. Part (6%) of the main laser pulse with a duration of 60 fs was used as an additional artificial pre-pulse. In this case, the delay varied from 20 to 80 ps, which made it possible to change the pre-plasma scale within the range of $10-50\lambda$. The electron energies reached ~ 1 MeV with a beam divergence of $20-40°$. The effect of the pre-pulse on the direction of propagation of electrons was experimentally discovered: In the absence of a delay between the pre-pulse and the main pulse, electrons were generated along the normal to the target surface; however, as the delay increased to 80 ps, the electrons propagated in the direction of the reflected laser pulse. However, the mechanisms of electron acceleration, as well as the effect of the pre-plasma, were not studied further in this work.

There is one more acceleration mechanism – vacuum laser acceleration (VLA) [117]. Using PIC simulations for VLA, it was demonstrated that electrons can reach energies of ~ 1 GeV upon injection of electrons with an initial energy of $10-20$ MeV in the field of a laser pulse with $I \sim 10^{22}$ W cm^{-2} [118]. Experimentally, such energies have not yet been achieved; the effect was experimentally confirmed for the first time in 2016 [119]. In this work, a laser pulse with a duration of 25 fs with a peak intensity of 2×10^{18} W cm^{-2} and a high contrast ($K_{ps} \sim 10^{-10}$ with a delay of 2 ps) achieved by using a double plasma mirror [120] was focused on an aluminium target at an angle $\theta = 55°$. To produce a pre-plasma on the target surface, a femtosecond laser pre-pulse with an intensity of $\sim 10^{16}$ W cm^{-2} was separated from the main pulse using a mirror. By varying the delay between the main pulse and pre-pulse, it was possible to change the pre-plasma scale L in the range $\lambda/3 - \lambda/30$; the optimal parameters were achieved for the gradient length $\lambda/15$. The generated electrons had an average energy of several MeV, a charge of ~ 12 nC, and a characteristic 'ring' spatial structure of the beam, which arises due to the ponderomotive repulsion of electrons by a laser pulse upon VLA. The influence of the characteristic scale of the pre-plasma on the generated beam has not been studied; however, from the information presented, it can be concluded that a very short gradient ($L \sim \lambda/6$ or less) is required to implement the VLA under such conditions.

The regime of grazing incidence of a laser pulse on a plasma is of great interest. Note that in many works on this topic, the scale of the pre-plasma inhomogeneity is not specified, which significantly complicates the interpretation of the results. For an intensity of $(1-2) \times 10^{18}$ W cm^{-2} at a pulse duration of 30 fs ($K_{ASE} \sim 10^{-5}$), Li et al. [121] showed that with an increase in the angle of incidence θ up to 70°, an electron beam is formed that propagates along the front surface of the target, with an energy reaching 2 MeV, and an angular divergence of less than 15°. To determine the role of the preplasma in the experiment, an additional pre-pulse was used – part of the main pulse before compression (duration 200 ps, delay 0.5 ps) with variable energy ($4-27$ mJ). It was shown that, as in Refs [28, 116], with the addition of a pre-pulse and an increase in its energy, the direction of propagation of the electron

beam gradually changes from the grazing one to the direction of the reflected laser pulse. Therefore, we can conclude that a short pre-plasma is required to form an electron beam along the target surface, but its exact scales are not indicated in the work.

The grazing incidence of a laser pulse was studied in more detail in Ref. [122]. The main pulse ($\varepsilon = 300$ mJ, $\tau = 67$ fs, $I \sim 10^{18}$ W cm^{-2}) and the pre-pulse (for the optimal case $K_{ns} \sim 10^{-4}$), the intensity of which was varied by changing the delay of the Pockels cells, interacted with the copper target at $\theta = 72°$. In the optimal case (the formation of a pre-pulse cloud of about 100 μm with a density $n_e = 0.1n_{cr}$), a stable and collimated (fluctuation of the beam emission angle $\sim 1°$, divergence 20 mrad) beam with a charge of 30 pC was obtained; a 'monoenergetic' peak was observed in the spectrum at an energy of 0.5 MeV. The simulation made it possible to draw a conclusion about the formation of the structure of the plasma 'bubble' (similar to that observed under wake acceleration) in a surface plasma wave excited in a plasma of near-critical density.

The grazing incidence regime can also be characterised by high (several orders of magnitude higher than in LWFA) coefficients of conversion of laser pulse energy into accelerated electrons [123]. Here, using PIC simulation, the interaction of high-intensity ($a_0 \sim 50-100$, $I \sim 10^{22}$ W cm^{-2}) radiation with a solid target was considered. It was shown that the addition of a pre-plasma layer with a density of tenths of n_{cr} makes it possible to increase the number of high-energy ($E > 10$ MeV) electrons by a factor of $2-5$. It should be noted that in this work the pre-plasma gradient was set by a linear function, which can be considered a very rough approximation to real conditions.

Generation of electron beams under oblique incidence of radiation on a target is also being investigated on laser systems with a relatively high energy and long pulse duration. For example, Ma et al. [107] used a pulse with a power of 200 TW ($\varepsilon = 150$ J, $\tau = 700$ fs, $I \sim 10^{18}$ W cm^{-2}, $K_{ns} \sim 10^{-4}$, $\theta = 72°$) and a pre-pulse with an energy of $5-80$ mJ ($I > 10^{16}$ W cm^{-2}, that is, inherently higher than the plasma formation threshold), interacting with a solid copper target. An electron beam with a charge of ~ 100 nC ($E > 1$ MeV), a divergence of 0.047 rad (2.7°), and electron energies up to 20 MeV was obtained in the direction of the reflected radiation. The effect of the pre-pulse (its energy, delay) on the parameters of the electron beam was studied. It was shown that an increase in the pre-pulse energy increases the divergence, but does not affect the beam charge; an increase in the charge is achieved only by increasing the energy of the main laser pulse. At the same time, the specific characteristics of the pre-plasma are not given in the work. PIC simulations have established that the acceleration mechanism is DLA [124], which ensures collimation of the electron beam.

Metal foils are also often used as solid targets. The use of foil makes it possible to generate beams of electrons (and ions) in the direction of propagation of the laser pulse. Yu et al. [125] considered theoretically the scheme of electron acceleration under the action of a high-intensity ($a_0 = 7.5$) laser pulse on a metal foil. A homogeneous pre-plasma layer with a thickness of 30 μm ($L \sim 30\lambda$) with a density of $10^{-3}n_{cr}$ was formed in front of the foil, in which electrons accelerated by the ponderomotive action

of a laser pulse were generated. The foil (a layer with a supercritical plasma concentration $n = 10n_{cr}$) reflected laser radiation, while electrons flew forward. In this case, the maximum electron energies were ~ 25 MeV. In the experimental work [126], an aluminium foil 7.5 μm thick was irradiated with a femtosecond pre-pulse with an intensity of 1.5×10^{17} W cm^{-2}, arising from the imperfection of the regenerative amplifier of the laser system, as a result of which a subcritical pre-plasma was formed (its scale was not specified in this work). Then, after a delay of 5 ns, the main laser pulse ($\tau = 70$ fs, $I = 2.5 \times 10^{18}$ W cm^{-2}) interacted with this pre-plasma and, as a result, a quasi-monoenergetic electron beam with energies of ~ 0.63 MeV and a divergence of $\sim 4°$ was generated in the direction of propagation of the initial laser radiation.

For thin foils, the effect of the pre-plasma gradient on the acceleration of electrons was also investigated using PIC simulation [127]. A high-power laser pulse with $a_0 = 10$, interacting with a solid-state target 20 μm thick, was considered. It is shown that, due to the high intensity, the laser pulse breaks through the foil and forms a channel in which the electrons are accelerated; the addition of a pre-plasma ($L/\lambda = 0.75$, $n = 1.5 \times 10^{19}$ cm^{-3}) leads to the appearance of a 'tail' in the spectrum of electrons, that is, to their additional acceleration, and therefore is an important parameter to consider.

Peebles et al. [128] showed that the addition of a controlled pre-pulse ($\tau = 2$ ns, $I = 2 \times 10^{12}$ W cm^{-2}) 4 ns before the arrival of the main pulse ($\tau = 150-600$ fs, $\varepsilon = 30-105$ J, $I \sim 10^{20}$ W cm^{-2}) on an aluminium target with a thickness of 100 μm allows one to increase by two orders of magnitude the number of high-energy electrons generating in the direction of the laser pulse. It is also shown that the surface currents of 'cold' electrons, which, in turn, strongly depend on the chosen angle of incidence of radiation on the target, can have a significant effect on the emission angle of accelerated electrons.

A rather complicated experiment is described in [129], where the thickness of the plastic and silicon film targets was $5-500$ nm. With such a thickness of the target, even a terawatt laser pulse ($\varepsilon = 1$ J, $\tau = 120$ fs, $I \sim 10^{19}$ W cm^{-2}, $K_{ns} \sim 5 \times 10^{-7}$, OPCPA system) pierces it through. It was shown that, with decreasing film thickness, a monoenergetic peak appears in the electron spectrum at an energy of ~ 2 MeV. Acceleration also occurs in the plasma channel; the energy peak is due to a 'bunch' of electrons injected into one accelerating phase of the laser pulse field. Due to the rather high intensity of the pre-pulse and the very small thickness of the target, the main pulse interacts with the pre-plasma cloud. From one-dimensional hydrodynamic simulation, the target density was estimated as a Gaussian 'bell' with a width of $1-5$ μm, depending on the initial thickness. It should be noted once again that this simulation does not describe the real picture reliably [80, 81] and can be used only for preliminary estimates.

Various composite targets are also being investigated. For example, Mandal et al. [130] used an 8-μm-thick PET film with a 50-nm-thick aluminium layer on the front and/or rear surfaces as a target. A laser pulse interacted with this target ($\tau = 30$ fs, $\varepsilon = 160$ mJ, $I \sim 10^{19}$ W cm^{-2}, $K_{ASE} < 2 \times 10^{-9}$, $\theta = 30°$). The obtained electron beams in all cases had a large divergence ($\sim 40°$), a charge of tens of pC, and an electron energy of up to 1 MeV. It was shown that the

presence of a metallic coating on the front surface ($L/\lambda \sim 0.6$) increases both the energy and the electron flux, while the presence of a coating on the rear surface ($L/\lambda = 0.1$) increases only the flux. The first effect is associated with a more efficient absorption of a laser pulse in a long metal pre-plasma, and the second, with the suppression of the ambipolar field on the rear side of the target due to the formation of a pre-plasma there. At the same time, estimates of the characteristic scale of the pre-plasma were also obtained using the hydrodynamic 1D code.

Gray et al. [78] investigated the acceleration of electrons during the interaction of a laser pulse ($\tau = 0.8$ ps; $\lambda = 1054$ nm; $\varepsilon \sim 130$ J; $I \sim 10^{20}$ W cm^{-2}; p polarisation; $K_{ASE} \sim 2 \times 10^{-12}$ and 2×10^{-10} with a delay of 1 ns and 100 ps, respectively; and $\theta = 19°$) with a thin composite target made of aluminium (40 µm), copper (8 µm), and CH (75 µm) in the presence of a long artificial pre-pulse ($\tau = 5$ ns, $\lambda = 1054$ nm, $\theta = 0$). The pre-pulse was ahead of the main pulse by 1.5 ns. The pre-pulse intensity varied from 0 to 23 TW cm^{-2} ($K_{ns} = 0 - 2.3 \times 10^{-7}$). At a pre-pulse intensity of ~ 2 TW cm^{-2} ($K_{ns} \sim 2 \times 10^{-8}$), a maximum of the efficiency of electron acceleration was observed and the yield of Kα radiation from a copper target increased sharply (approximately fourfold), as well as the efficiency of conversion of the laser pulse energy into the kinetic energy of protons (from $\sim 0.5\%$ to 3%) and the maximum energy of these pro-

tons (from 7 to 22 MeV). A further increase in the pre-pulse intensity led to a sharp decline in the conversion efficiency (at an intensity of 4–5 TW cm^{-2}) and then to its slow recovery. Simulation with the PIC code EPOCH showed that in the presence of a pre-plasma, the laser beam undergoes self-focusing and a plasma channel is produced in which electrons are efficiently accelerated. However, with an increase in the pre-pulse intensity, the electron density of the plasma increases near the focal point of the main pulse, which leads to the breakup of the channel into separate filaments, to rapid dissipation of the beam energy, and a decrease in the efficiency of electron acceleration. Two regions of generation of high-energy electrons were observed: the region of self-focusing of the beam in the pre-plasma and the region with a density close to the critical one. A similar picture of laser-plasma interaction was observed in Refs [65, 66] when studying the dependence of the temperature of electrons generated from the rear surface of a thin-film target on the intensity of a long pre-pulse that forms a pre-plasma layer.
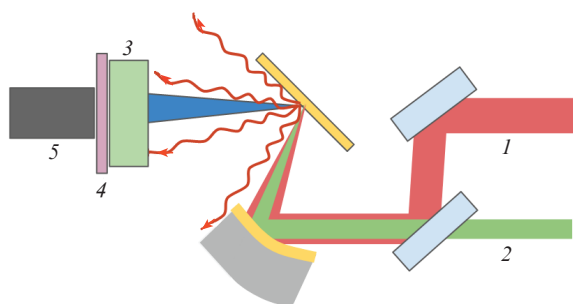
The possibility of electron acceleration by circularly polarised laser pulses was also considered (before that, p-polarised laser pulses were used in all the papers discussed). Liu et al. [131] describe the mechanism of self-consistent resonant acceleration of electrons in the channel (that is, betatron acceleration by circularly polarised radiation). In the simulation, a laser pulse with $I \sim 10^{20}$ W cm^{-2}
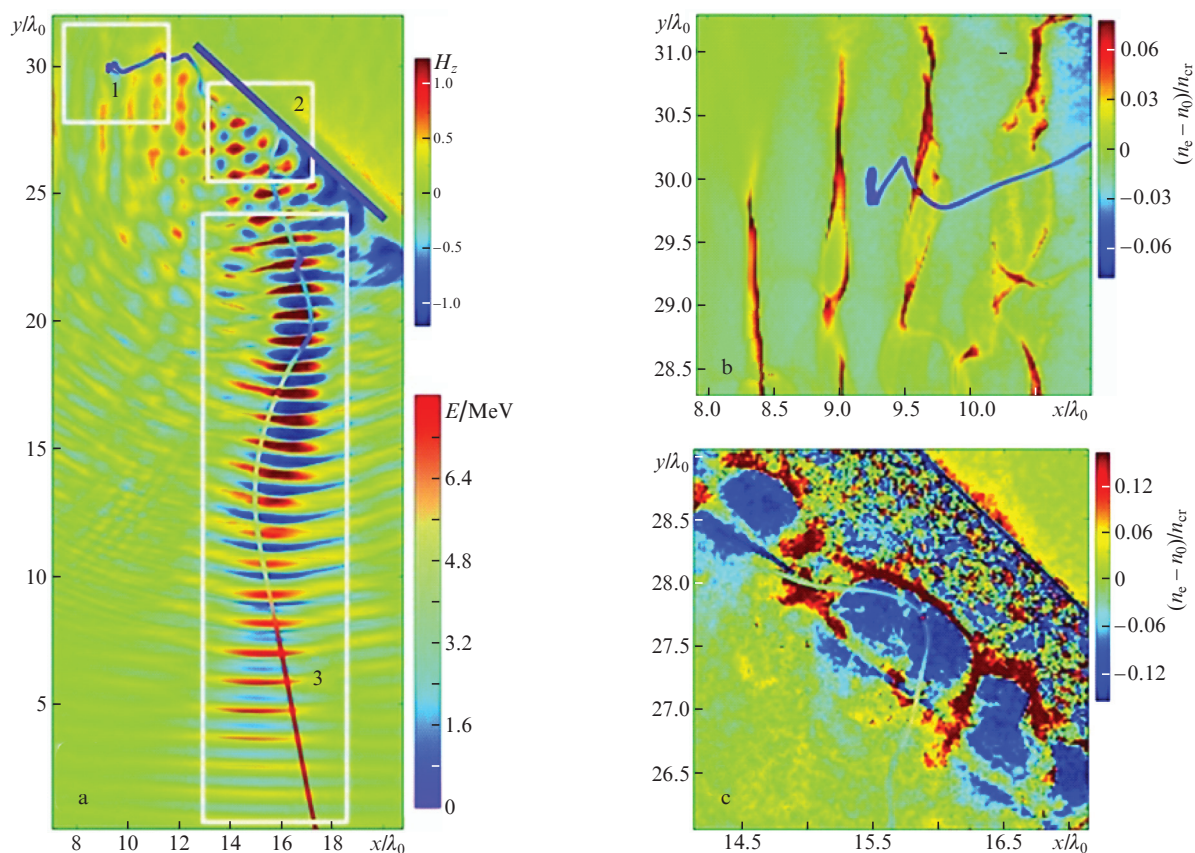
Figure 4. (Colour online) (a) Magnetic field of the laser pulse H_z (normalised to a_0) (a) and (b, c) deviation of the electron density from the equilibrium $n_e - n_0$, showing the plasma waves of parametric instabilities (b) at the moment of their breaking and the beginning of electron acceleration and (c) at the moment of injection into the plasma channel (densities are normalised to n_{cr}). The figures also show the trajectories of the test electron. The colour of the trajectory corresponds to the electron energy E (shown on the vertical colour scale). The purple line in Fig. 4a corresponds to the critical electron density n_{cr}.

was incident along the normal to the target, which was set in the form of a plasma with an electron density linearly increasing from 0 to n_{cr} over a length of 5 µm; further on, the concentration remained constant. At the same time, in this work, the role of the pre-plasma gradient was not investigated. The use of circular, rather than linear, polarisation of the fundamental radiation led both to an increase in the number of electrons injected into the channel and to a better collimation of the generated electron beam due to the specific shape of the magnetic fields formed in the plasma. Electron energies of 250 MeV are also higher for circular polarisation (200 MeV for linear polarisation). In addition, to improve the parameters of the electron beam, it was proposed to use two successive laser pulses with a controlled delay (several picoseconds) and a ratio of focal spot diameters (~3 in the optimal regime) [132].

Thus, the length of the plasma layer L plays a crucial role in the formation of high-energy electron beams. In a series of papers [113, 133, 134], it was shown how a properly selected contrast, which is determined by a combination of pre-pulses of a femtosecond laser system and a pulse of a separate nanosecond laser, can form a plasma profile with the required steepness, 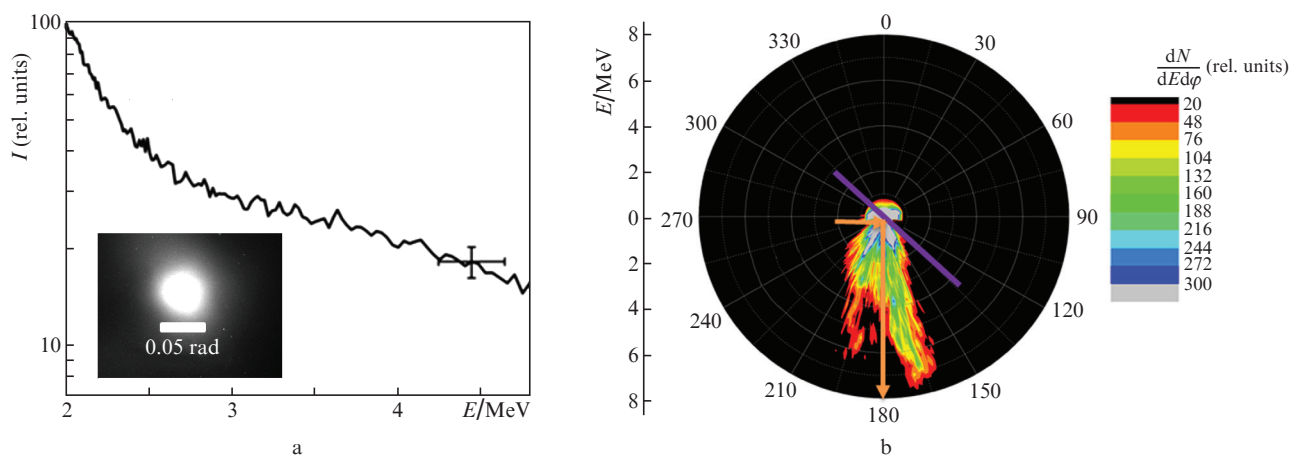which makes it possible to optimise the parameters of an electron source. In these works, a large amount of experimental data was presented and numerical PIC simulation was performed, which made it possible to outline a picture of the physical processes leading to the formation of a collimated beam of relativistic electrons in the direction of the reflected laser radiation and to optimise the parameters of this beam.

Three stages of acceleration are identified: the growth of hybrid plasma instability [SRS and two-plasmon decay (TPD)] and the excitation of plasma waves in the region with $n_e = 0.25 n_{cr}$ (stage 1), the initial energy gain by some of the electrons and their injection in the direction of the reflected laser pulse due to the breaking of plasma waves (stage 2) and and electron acceleration in the DLA regime in a channel formed in a rarefied plasma by a reflected laser pulse (stage 3) (Fig. 4). This takes place if a specially prepared plasma profile, consisting of a sharp section near $(0.1–0.5)n_{cr}$ and a smooth decrease in the region of lower densities [$n_e = n_0 e^{\xi/(0.5\lambda)} + n_1 e^{\xi/(10\lambda)}$, where ξ is the coordinate along the normal to the target surface; and n_0 and n_1 are fitting parameters).

In the experiment performed by Tsymbalov et al. [113], such a plasma is produced by a separate nanosecond laser pulse, with the femtosecond pulse arriving at the maximum intensity of the nanosecond pulse. The intensity of the latter must be sufficient (5×10^{12} W cm^{-2}) so that the ponderomotive forces arising during its reflection from the plasma lead to its steepening to $L \sim 0.5\lambda$. The steepening occurs near the region of the critical electron density, where the femtosecond laser pulse is reflected. An increase in the scale of the plasma inhomogeneity in this region leads to strong absorption and scattering of the laser pulse. Such a reflected pulse cannot produce a plasma channel, and the acceleration occurs by the VLA mechanism with a greater divergence and lower energy and charge of the electron beam. Simulations [113] showed that an increase in the slope to $L \sim 0.25\lambda$ leads to a decrease in the electron beam current by about a factor of two. This is due to the smaller plasma volume from which the electrons enter the channel and the injection mechanism itself. Thus, the optimal plasma length in the range $(0.1–0.5)\,n_{cr}$ is 0.5λ.

Figure 5. Simplified scheme of the experimental setup: (*1*) radiation from a Ti:sapphire laser system; (*2*) Nd:YAG laser radiation (controlled pre-pulse); (*3*) permanent magnets of the spectrometer ($B \sim 0.15$ T); (*4*) Kodak LANEX scintillator; (*5*) CCD camera.

Figure 6. (Colour online) (a) Spectrum of electrons with a temperature of 2.1 ± 0.5 MeV and visualisation of an electron beam on a scintillator (inset), as well as (b) the distribution of electrons over energies and emission angles, obtained during simulation for conditions corresponding to the experiment. The electron beam divergence obtained in the simulation is 0.05 rad, and the spectrum temperature is 2 MeV. The purple line in Fig. 6b corresponds to the position of the target surface, and orange arrows show the directions of the incident and reflected laser radiation.
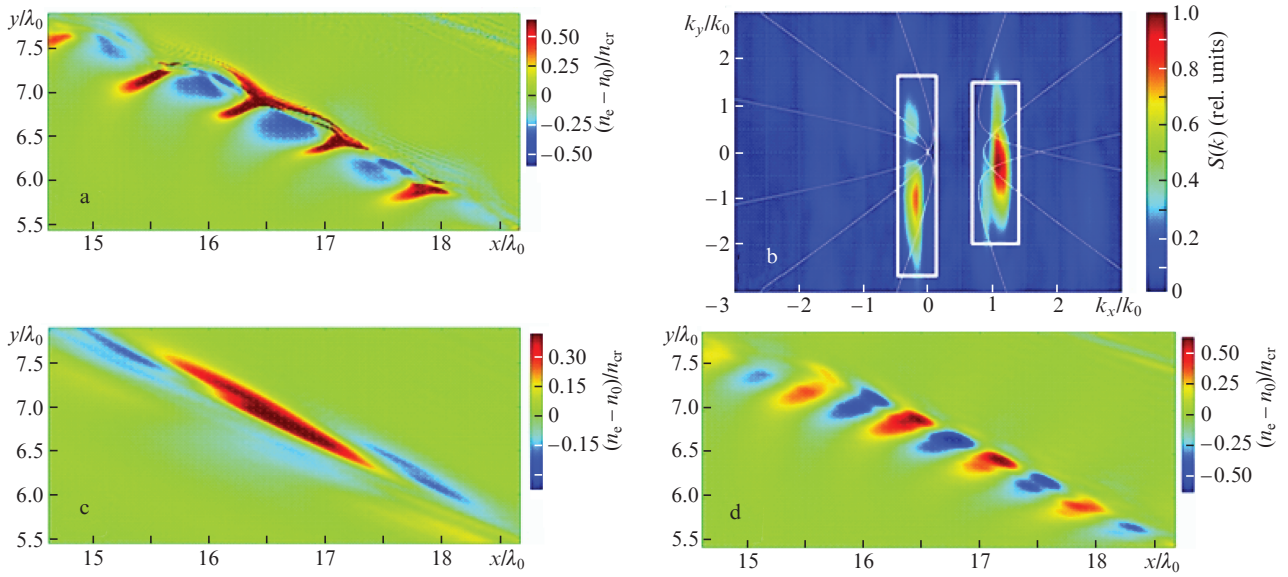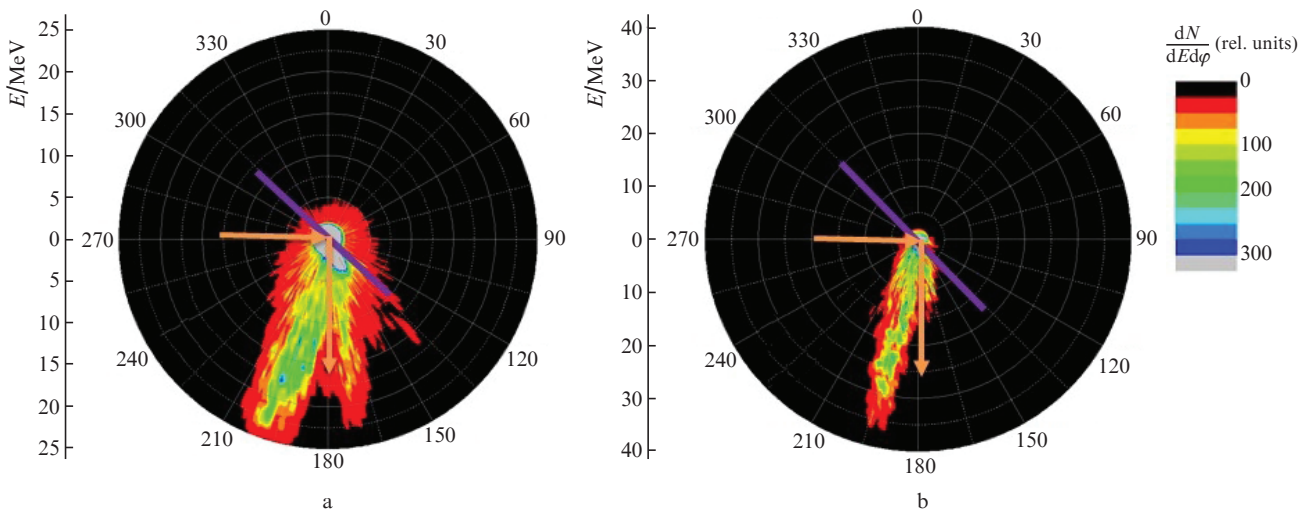
Figure 7. (Colour online) (a) Deviation of the electron density from the equilibrium $n_e - n_0$, (b) the spectral power density $S(k)$ of plasma waves (white rectangles show the filtration regions), (c) the electron density after filtration in the vicinity of $k_x \approx 1.1\omega_0/c$, $\Delta k_x \approx 0.5\omega_0/c$, corresponding to a plasma wave common for TPD and SRS instabilities, and (d) the electron density after filtration in the vicinity of $k_x \approx -0.2\omega_0/c$, $\Delta k_x \approx 0.5\omega_0/c$, corresponding to the second plasma wave of TPD. Results are presented for an incidence angle of 60°. The densities are normalised to n_{cr}.

It was experimentally shown that in this regime, it is possible to generate a collimated (divergence $\sim$0.05 rad) electron beam with a temperature of 2 MeV and a charge of tens of pC on a 1-TW laser system. The schematic of the setup is shown in Fig. 5: the main laser pulse of the Ti:sapphire laser system ($I \sim 5 \times 10^{18}$ W cm^{-2}, $\varepsilon = 50$ mJ, $\tau = 50$ fs, $K_{ASE} \sim 10^{-7}$) and the controlled pre-pulse of the additional Nd:YAG laser ($I \sim 5 \times 10^{12}$ W cm^{-2}, $\varepsilon = 200$ mJ, $\tau = 10$ ns) were incident on a thick (2 mm) solid tungsten target at an angle $\theta = 45°$. The spatial distribution of electrons was recorded using a LANEX scintillator installed in the direction of reflection and a CCD camera transmitting its image.

To measure the energy spectrum, two permanent magnets (magnetic field strength $\sim$0.2 T) were placed in front of the scintillator. The profile of the electron beam and its energy spectrum are shown in Fig. 6a. The data on the beam charge are confirmed by the registration of neutrons in the photonuclear reaction [113]. The obtained beam characteristics are in good agreement with the results of numerical simulation shown in Fig. 6b.

Based on the simulation of the motion of test electrons in a given field, the optimal initial parameters were obtained, leading to obtaining the maximum energy at the plasma channel end. It was shown that electrons should enter the

Figure 8. (Colour online) Numerical simulation results: distribution of electrons in the energy–emission angle space for a laser pulse power of (a) 10 and (b) 40 TW. The purple line corresponds to the position of the target surface, and orange arrows show the directions of the incident and reflected laser radiation.

channel with an initial energy of several hundred keV in the maximum of the envelope of the laser pulse propagating in the channel. Simple estimates show that plasma waves of hybrid SRS–TPD instability are capable of generating electrons with the required energies. This instability generates two groups of waves [134]: One moves along the plasma surface ($k \approx 1.1\omega_0/c$), while the other moves approximately along the normal to this surface ($k \approx 0.2\omega_0/c$), with the phase velocity directed towards the plasma region with lower density. Figure 7 shows the deviation of the electron density from the equilibrium one; one can see the existence of plasma waves (Fig. 7a), the spatial spectrum of these plasma waves (Fig. 7b) and the modulation of the electron density corresponding to the first (Fig. 7c) and the second (Fig. 7d) plasmons, obtained as a result of spatial Fourier filtering in the regions marked in Fig. 7b. A detailed analysis of the development of this hybrid SRS–TPD instability is given in Ref. [134].

Analysis of the electron motion during PIC simulation showed that the first group of waves accelerates electrons, and the fields of the second group of waves eject electrons in the direction of the plasma channel. Thus, the electrons generated by the decay of plasma waves of hybrid instability are injected into the plasma channel formed by the reflected laser pulse.

In addition, the possibility of generating electron beams during the interaction of a laser pulse with a layer of a dense plasma was investigated. It was shown [133] that plasma waves of parametric instabilities arising in a thin plasma layer with $n_e = 0.15-0.3n_{cr}$, during their decay, can effectively inject electrons into the field of a laser pulse transmitted through the layer. Trapped electrons are accelerated by the DLA mechanism in a plasma corona dense enough to produce a channel. In this case, the same collimated (0.05 rad) electron beam is generated as in the case of reflection from a solid target described above. However, the total charge of electrons with energies above 1.6 MeV is 50 pC. Thus, the injection efficiency and, accordingly, the charge of the generated electron beam increases by a factor of ~ 5 compared to injection into the reflected laser pulse at the same pulse energy (50 mJ) of the initial laser beam. The calculations are confirmed by experiments using plastic films, preionised by an additional nanosecond pulse, as a target. In this case, photonuclear techniques were also used to measure the electron beam charge.

Thus, Tsymbalov et al. [113, 133, 134] showed that an artificial nanosecond pre-pulse with an intensity of $\sim 10^{12}$ W cm^{-2} and a high intrinsic contrast ($K_{ASE} \sim 10^{-8}$) of the main laser system can significantly increase the energy and charge and reduce the divergence of electron beams. The results described above were obtained using a laser system with a peak power of 1 TW. It is interesting to establish the range of intensities in which the above model of injection and acceleration works. Simulations were performed for intensities of 5×10^{19} W cm^{-2} and laser beam diameters at FWHMs of 4λ and 8λ. The electron energy and angle distributions in the obtained beams are shown in Fig. 8. At peak laser pulse powers of 10 and 40 TW, well collimated beams with maximum electron energies of up to 25 and 40 MeV, respectively, can be obtained. The use of such laser systems will require a

higher contrast (better than 10^{-9}) due to the increased intensity, but this is conceivable for existing laser systems [114]. At intensities exceeding 5×10^{19} W cm^{-2}, the light pressure becomes so high that electrons are ejected from the interaction region without having time to form plasma waves, and the parametric processes necessary for effective injection are suppressed. Therefore, a further increase in the laser intensity to increase the yield and electron energies is not optimal; it is better to increase the beam diameter, which will make it possible to increase the injection area, as well as the acceleration length due to the lower divergence of the wider beam.

The direct electron acceleration (DLA) mechanism is experimentally observed at high intensities and laser pulse durations. Rosmej et al. [135, 136] used a low-density foam with a thickness of several hundred micrometres as a target, which, upon interaction with a controlled pre-pulse ($\tau = 1.5$ ns, $\varepsilon \sim 1-3$ J, $I \sim 10^{13}$ W cm^{-2}), was transformed into a plasma of near-critical density. The interaction of the main pulse ($\tau \sim 750$ fs, $\lambda = 1053$ nm, $\varepsilon \sim 90$ J, $I \sim 10^{19}$ W cm^{-2}, s polarisation, and $\theta \sim 5°$) with this preformed plasma led to the acceleration of electrons, and a significant increase in the beam charge and spectrum temperature was observed in comparison with the case of using conventional foil targets at $I \sim 10^{21}$ W cm^{-2}, which is due to the longer acceleration length (that is, the presence of a plasma channel).

5. Role of the contrast of laser radiation during ion acceleration

The acceleration of protons, deuterons, and multiply charged ions by high-intensity femtosecond laser radiation is of considerable fundamental and applied interest [7, 17, 137]. Such laser-accelerated ion fluxes can be used in the production of semiconductor and membrane materials, in the colorisation of crystals, and for laser plasma diagnostics [138, 139], including for time-resolved diagnostics of plasma electric fields with a short pulse of fast protons [140]. It should also be noted that the use of laser-accelerated fluxes of electrons and ions with high energy, as well as X-ray radiation in nuclear photonics [141], is promising for the excitation of nuclear (including isomeric) levels [142], initiation of thermonuclear reactions [143] and fission reactions [142], and obtaining fast neutrons using photonuclear [98] or nucleon transfer reactions [144]. An important and promising area of research is medical applications: hadron therapy of oncological diseases [145], production of isotopes for positron emission tomography [146], etc. Note that hadron therapy usually requires energies of hundreds of MeV per nucleon [147].

The first review devoted to laser acceleration of ions was published back in 1986 [148]. It discussed mainly measurements utilising nanosecond CO_2 lasers, as well as the first theoretical models of ion acceleration. The radiation intensity on the target reached 10^{16} W cm^{-2}, which ensured the acceleration of protons and carbon ions to energies of several tens of keV. At present, using femtosecond (30–100 fs) laser pulses with an energy of up to 1 J and a peak intensity on a target of $(1-5) \times 10^{19}$ W cm^{-2} and ultrathin targets, protons and multiply charged heavy ions with energies of ~ 100 MeV per nucleon were obtained [149, 150].

When the beams of accelerated electrons are formed, only a small part of the electron subsystem is involved in this process. On the contrary, the acceleration of ions is associated with the motion of the plasma layers as a whole. This acceleration is associated with the charge separation inside the plasma under the action of the forces of electron pressure and, in part, the action of laser radiation [151, 152]. The emerging ambipolar field accelerates the ions, while slowing down the escaping electrons. As a result, the charge separation region moves with acceleration, which determines the acceleration of ions as a whole. In the interaction regimes considered in this review, there is, as a rule, a complex electron energy distribution, which is conventionally divided into several components with different average energies E_{hot}. According to a rough estimate, the value of the ambipolar field for each of the components is $F_a \sim E_{hot}/(e\lambda_D)$, where λ_D is the Debye radius. These fields can exceed 10^{12} V m^{-1}. When thick targets are used, ions are accelerated towards the laser beam, approximately along the normal to the plasma–vacuum interface. For thin-film targets, ions can be accelerated from the rear side of the film under the action of a beam of electrons accelerated into the depth of the target by a laser field. This mechanism is called target normal sheath acceleration (TNSA) (that is, acceleration by a near-surface layer of heated electrons) [7, 153].

In the early studies of laser acceleration of ions, it was found that the most efficiently accelerated (due to the maximum charge-to-mass ratio) are protons, as well as carbon and oxygen ions from the natural layer of hydrocarbon contamination on the target surface [148]. In this case, the accelerating near-surface layer of light ions (mainly protons) screens the ambipolar field, preventing the acceleration of heavier multiply charged ions. To weaken this effect, it is necessary to remove the surface layer consisting of light atoms before the interaction. This is achieved by thermal or laser heating of the target surface or by ablation [154–158].

The contrast of laser radiation has a decisive influence on the characteristics of the formed ion beam. First, the use of thin-film (up to tens of nanometres) targets dictates the need for high contrast so that the target is not evaporated before the main pulse is applied [159]; second, the presence of a long but weak ASE or even a multitude of weak pre-pulses can lead to the formation of a heated, expanding and less dense plasma, in which the acceleration of ions is much less effective [160]. In addition, Schollmeier et al. [160] showed that a significant discrepancy between the experimental results (for example, the cutoff energy for protons at an ideal Gaussian momentum is 150 MeV, and in the experiment it is equal to 50–60 MeV) is due to the overlooking of ASE in numerical simulations, and only if it is taken into account, it is possible to reconcile the experimental and calculated results.

It was experimentally demonstrated in [161] that the main laser pulse ($\varepsilon = 2$ mJ, $\tau = 50$ fs, $I \sim 10^{17}$ W cm^{-2}) having a weak short pre-pulse (10^{11} W cm^{-2}) ahead of it by 10 ns and arising due to the imperfection of the Pockels cells and, accordingly, providing a low contrast ($K_{ns} \sim 10^{-6}$) suppresses the acceleration of protons from the contaminating layer; in this case, heavy multiply charged iron ions experience a noticeable acceleration to energies

exceeding the average energy of hot electrons. Numerical simulation of this process, carried out in [161], showed that the predominant acceleration of heavier ions can occur if protons are removed from the target surface using a pre-pulse and, in this case, the spatial distribution of protons is nonmonotonic (there is a gap of ~ 2 μm between the proton layer and the target surface, which, for example, can occur due to explosive boiling up of the contaminating layer by a weak pre-pulse). In this case, the main pulse interacts with a cleaned but slightly heated target surface, and heavy multiply charged ions begin to accelerate more efficiently; meanwhile, protons experience weak acceleration by the exponentially decaying tail of the ambipolar field.

The target cleaning effect observed in Ref. [161] is achieved only for thick absorbing targets (that is, metals). In addition, the pre-pulse should be short enough to provide explosive boiling of the contaminant layer. When the intensity of a short prepulse exceeds the ablation threshold of a metal target, the proton density profile, which is established due to the action of the pre-pulse, becomes exponential, and the main pulse accelerates protons rather than heavy ions. On the other hand, if the intensity of the pre-pulse is insufficient to completely remove the contaminating layer, then the remaining protons are effectively accelerated by the main pulse, and heavy ions gain a significantly lower energy.

A similar mechanism for cleaning the target surface can be realised under the action of ASE. Shulyapov et al. [162] showed that when using metal targets and the intensities of the main pulse and ASE $\sim 2 \times 10^{18}$ and $\sim 10^{10}$ W cm^{-2}, respectively ($K_{ASE} \sim 10^{-8}$ with a delay of 10 ps), the target is effectively cleaned from protons and the efficiency of acceleration of heavy ions is increased. (When using a contrast enhancement system (XPW) providing $I_{ASE} < 10^8$ W cm^{-2} ($K_{ASE} < 10^{-10}$), the target is not cleaned.) The advantage of this cleaning method is to use only one laser system without any additional equipment; on the other hand, controlled target cleaning is only possible with an additional artificial pre-pulse.

For targets in the form of a thin foil, sufficiently intense pre-pulses and ASE can generate a shock wave that propagates into the target and leads to expansion and deformation of its rear side, changing the spatial distribution of the quasi-static electric field, which accelerates ions by the TNSA mechanism [163–166]. Fuchs et al. [167] showed that even for relatively thick targets (aluminium foil 20 μm thick), with the addition of a controlled pre-pulse ($I \sim 10^{16}$ W cm^{-2}) 8 ns before the arrival of the main pulse, a plasma corona can be formed on the rear surface of the target. (Similar results are also discussed in [153] for aluminium foils up to 20 μm thick and ASE with $I \sim 10^{12}$ W cm^{-2} ($K_{ASE} \sim 10^{-7}$).) This leads to a smoothing of the electron density gradient and suppression of the TNSA efficiency [153].

It was shown in [168, 169] that at $I_{ASE} \sim 10^{10}$ W cm^{-2}, even a slight deformation of the rear side of the target can reduce the ion energy, and Fang et al. [170] found that the deformation of the rear side (at $I_{ASE} \sim 10^{12}$ W cm^{-2}), in addition to decreasing the energy of protons, can increase the divergence of the proton beam. In addition, the contrast of laser radiation also affects the efficiency of ion acceleration (that is, the coefficient of conversion of the energy of

laser radiation into the energy of accelerated particles) [171]. In particular, Yogo et al. [172] investigated the effect of the ASE duration (with a rather poor contrast, $K_{ASE} \sim 10^{-5}$) on the emission angle and energy spectrum of protons using a relatively thick foil (7.5 µm).

The optimal target thickness for efficient acceleration of protons depends not only on the parameters of the laser pulse, but also on the target density. For a significant number of previously published works on ion acceleration, K_{ASE} was $10^{-5} - 10^{-8}$ (that is, it was below or near the plasma formation threshold on the front surface of the target) and, therefore, for frequently used aluminium foil targets with a thickness of 1 µm, the deformation of the rear surface the target could be neglected [173]. In studying the interaction of a laser pulse ($\varepsilon = 600 - 850$ mJ, $\tau = 150$ fs, $I \sim 10^{19}$ W cm^{-2}, and $\theta = 30°$) with aluminium foils of various thicknesses, Kaluza et al. [166] showed that for pulses with $K_{ASE} < 10^{-7}$ ($I \sim 10^{12}$ W cm^{-2}), the optimal target thickness for accelerating protons decreases with decreasing ASE duration (with a minimum ASE duration of 0.5 ns, the optimal thickness of the aluminium foil was 2 µm, and the proton energy was $\sim$3.5 MeV). In this case, for thinner targets, the spatial profile of the proton beam became blurred, which was associated with the deformation of the rear surface of the target.

Fast heavy carbon ions with the highest energy are produced using homogeneous carbon targets. At the same time, as already noted, the presence of hydrogen, distributed in the form of a contaminant layer on the rear surface, greatly reduces the efficiency of accelerating carbon ions. Removal of hydrogen-containing contamination from the rear surface of the target increases the efficiency of acceleration of heavy ions [154, 156, 174, 175]. In contrast, a target with a high atomic number and a hydrogen-containing layer on the rear surface is best suited for optimising proton acceleration [175]. It should be noted that, as a rule, the thickness of the hydrogen-containing layer on the target surface is 2–4 nm. Simulation with layers up to 100 nm thick [176–178] could lead to unrealistic results (mainly from the point of view of the obtained energy spectrum) [179].

An already preionised target in the form of a thin subcritical plasma can also be used to accelerate ions. For example, Matsukado et al. [180] observed protons accelerated from a thin foil target, the laser-irradiated region of which was evaporated by ASE with the formation of a plasma profile with a maximum density close to the critical [181], and Willingale et al. [182] demonstrated effective laser acceleration of ions with a target in the form of a dense gas jet.

The above results refer to the interaction regime, when the laser radiation intensity is in the range of $10^{18} - 10^{20}$ W cm^{-2}, and the target thickness exceeds 50 nm. In this case, the TNSA mechanism is dominant [183], with the maximum ion energy increasing with decreasing target thickness. At the same time, other acceleration mechanisms come to the fore for ultrathin targets and ultrahigh contrast laser pulses with an intensity above 10^{20} W cm^{-2} [7]. For example, Bulanov et al. [184] demonstrated the essential role of the effect of relativistic transparency in the transfer of energy from a laser pulse to ions. Numerical simulations and experiments carried out with ultrathin targets and laser pulses with an intensity of $10^{20} - 10^{24}$ W cm^{-2} with a contrast of more than 10^{-12} indicate the possibility of a signifi-

cant increase in ion energy with a narrower energy spectrum; however, poor contrast significantly impairs the efficiency of ion acceleration, reducing their maximum energy and strongly cutting off the low-energy part of the spectrum [185].

The interaction regimes, including break-out afterburner (BOA) [186], directed Coulomb explosion [184], and radiation pressure acceleration (RPA) [187] are discussed in the literature. Ultra-high intensities (more than 10^{21} W cm^{-2}) at an ultra-high contrast of a pulse with a sharpened leading edge, necessary for the implementation of these acceleration mechanisms, were obtained quite recently using the most modern laser systems, which is one of the most important factors in the development of research on laser acceleration of ions.

Note that in some cases (for example, when high-density gas jets are used as targets), the presence of a pre-pulse with a certain duration is necessary to obtain a very sharp plasma – vacuum boundary [188] or to form a sharp boundary by shock waves induced in a dense gas jet by nanosecond laser pulses [189].

6. Interaction of laser radiation with structured targets

In experiments on relativistic laser-plasma interaction, specially prepared targets with a structured surface are also used to increase the absorption of laser radiation in the plasma and to increase the energy of accelerated particles. The first works were carried out at moderate intensities (up to $\sim 5 \times 10^{17}$ W cm^{-2}). A number of pioneering studies can be mentioned, where, due to the use of micro- and nanostructures of various types (porous targets [51, 190, 191], ordered diffraction gratings [192], weakly ordered nanowires and lamellas of various profiles [193–197] and even bacteria [198]), it was possible to achieve almost one hundred percent absorption of laser radiation, a significant increase in the energy of electrons in the plasma, and the yield of hard (bremsstrahlung and linear) X-rays.

To explain these results, several hypotheses have been put forward, including plasmon effects [199, 200], amplification of the local field near inhomogeneities of the order of a wavelength or less [195], an increase in absorption on an increased surface area [193, 201], and efficient generation of hot electrons by the mechanism of vacuum heating on a highly developed surface [202]. Note that the effects associated with surface plasma waves relate, rather, to the region of relatively low intensities (up to 10^{16} W cm^{-2}), when the mechanisms of inverse bremsstrahlung absorption prevail without the appearance of a significant population of the hot electron component. Nevertheless, even at such intensities, various resonance phenomena caused by the periodicity of the surface can lead to the appearance of high-energy particles, as shown in Ref. [199], where gold ions with energies up to a few MeV were detected. Recent studies [203–205] indicate the existence of surface plasma waves at relativistic intensities (over 10^{19} W cm^{-2}), when they contribute to an increase in absorption, an increase in plasma instabilities, and an increase in the energy of fast electrons. A significant influence of the effect of local field amplification on the efficiency of generation of fast electrons and ions in the presence of subwavelength structures has been found [195, 205–207].

Nevertheless, it is worth noting the significant fragmentation and lack of systematisation of the results obtained in different experiments. The reason for this may be insufficient control of the parameters of the laser pulse and, first of all, of the contrast. Thus, the authors of papers [50 – 52, 208] point to the role of the influence of pre-pulses on the efficiency of conversion of the energy of a laser pulse into X-ray radiation. In Refs [50, 53, 54, 209], a reduced resistance of nanostructures to ablation and melting is noted, which is associated with an increased absorption of radiation and a limitation of the outflow of heat into the depth of the target. In numerical simulations, it is also important to take into account three-dimensional effects, which can be decisive in the case of a complex target structure [210], but this is difficult due to limited computational capabilities.

Over the past decade, there has been a significant breakthrough in several directions at once. First of all, it is worth noting the development of laser technologies, which ensured the commercial availability of laser systems of multi-terawatt power with an extremely high contrast (better than 10^{-10}) and a high pulse repetition rate [211 – 215]. Due to this, the range of intensities for possible practical application of structured targets has expanded to relativistic intensities and higher (more than 10^{19} W cm^{-2}). An important role was also played by the development of methods for fabricating structures: 3D printing, lithography, chemical etching and deposition, and laser ablation make it possible to fabricate structures with completely different morphologies (both ordered and chaotic) and sizes of individual structural elements from tens of nanometres to tens of micrometres [216 – 223]. Finally, an increase in computing power made it possible to numerically investigate the effect of relativistically intense laser pulses on subwavelength structures, in which new mechanisms and effects of charged particle acceleration and even quantum electrodynamics were predicted [210, 224 – 229].

A wide range of tasks associated with the use of micro- and nanostructured targets in laser-plasma experiments can be conditionally divided into several areas, united by the common possibility of using the obtained source for various applied and fundamental research. The first area is associated with obtaining a bright source of hard X-ray radiation. The possibility of generating high harmonics and terahertz radiation should also be mentioned; however, here we discuss relatively low intensities and low energies of particles, and therefore this scope of work will not be mentioned further in this review. The second area includes work on accelerating electron and ion beams to high energies. Another area is related to the initiation and study of nuclear processes: the generation of neutron fluxes as a result of fusion reactions, decay and excitation of nuclear levels, etc. Finally, exotic and not yet experimentally realised quantum electrodynamic effects at ultrarelativistic intensities, up to the production of electron – positron pairs are being discussed [230]. All these areas will be considered in more detail after a brief discussion of methods for fabricating structured targets and the features of structures.

6.1. Methods for fabricating structures

Methods for micro- and nanostructuring of the surface are being developed for solving problems not related to laser-plasma interaction. Periodic structuring is important in problems of photovoltaics, nano- and microelectronics, microfluidics, biosensorics, etc. [231, 232]. Methods for the formation of structures can be conditionally divided into two types: (i) when the growth of structures proceeds from the surface into the depth of the material and (ii) when the structures grow from the surface upwards. The first type includes various methods of etching, when structures are formed by 'eating away' the target material, while chemical, laser, thermal and vacuum deposition, etc., are based on 'growing' structures on a substrate by different methods.

Crystalline silicon is one of the first materials with a modified surface that is successfully used in laser-plasma experiments. The most common methods for producing complex surface morphology on semiconductors are based on chemical etching of a smooth substrate. Thus, owing to its high photoluminescent properties, porous silicon has become widespread and, as a consequence, has a well-developed manufacturing technique [233]. Varying the etching parameters allows one to change the degree of porosity, pore size, and the depth of the etched layer. In laser-plasma experiments, porous silicon was used at the dawn of the development of this field [52, 191]. During vacuum heating, strong absorption of radiation and efficient generation of hot electrons were observed at the sharp boundaries of the developed surface [202].

Further development of techniques has led to the emergence of many methods of etching semiconductors. Nevertheless, one of the simplest and most effective is metal-stimulated etching [218, 234], which, in particular, makes it possible to achieve better local repeatability of the surface morphology that plays an important role in the discussed experiments. The most widespread type of structures obtained in this way is silicon nanowires (or nanograss) [218, 234]. In contrast to porous silicon, nanowires are much more ordered. In addition, they form an array of nearly identical structures. In this case, the height of the nanowires, their inclination relative to the substrate, and their diameter can vary over a wide range (from tens of nanometres to micrometres). From the point of view of laser-plasma research, this opens the way to the experimental implementation of ideas and concepts developed in the numerical simulation of the effect of a high-intensity laser pulse on matter. Thus, interesting results have been achieved by using both nanowires of submicron size [235] and structures whose size exceeds the wavelength [236] as targets for laser-plasma experiments.

The advantages of etching and the growth of structures from the surface into the depth include the possibility of etching a large area, a high aspect ratio of the height to the diameter of the forming structures, and also the fact that the structures are nothing more than the substrate remaining after etching, which provides a relatively high thermal conductivity in the depth of the target. The disadvantages of the etching method include the complexity of the forma-

tion of single wires, when the distance between adjacent ones approaches the same laser wavelength, while maintaining a high aspect ratio.

The methods of growing structures that can be used in laser-plasma experiments include laser ablation, electrochemical, thermal and vacuum deposition, and 3D printing.

Strictly speaking, laser ablation and the related processes of surface structuring cannot be attributed to a process in which particles of matter are deposited on the substrate from the outside, but at the same time the very formation of structures proceeds from the surface of the substrate into vacuum. The consideration of the mechanisms of the formation of nano- and microstructures during laser ablation is a problem to which a separate review can be devoted. In general, we are talking about the interference of the incident laser radiation and the surface electromagnetic wave excited by it. Within the framework of this work, we will restrict ourselves to only mentioning the fact that the formation of structures is quite simple and does not require complex technical solutions. In this case, it is possible to modify substrates from almost any material. At the same time, due to the complexities of the physics of the process and its modelling, it is very difficult to achieve good reproducibility from sample to sample. The structures themselves can take various forms (from individual pyramids, cones to complex, fractal-like formations), but have a relatively small aspect ratio [219, 237, 238]. Irradiation of the structures formed in this way by high-power femtosecond radiation also turned out to be promising [235, 236, 239]. Separately, it is worth noting work [240], in which the authors showed that structures that improve the parameters of laser plasma (in particular, an increase in the energy of protons) can be created by laser ablation with the same laser radiation (weakened to an energy density of ~ 5 J cm^{-2}) directly before the experiment, that is, without replacement or special preparation of the target. This approach is extremely promising for future experiments at a high (several kHz) pulse repetition rate.

Electrochemical deposition in an acid solution or in a vacuum [223, 241–243] is based on the growth of structures (wires, fibres, etc.) on condensation centres (micro- and nanodroplets of various elements) on the substrate surface. In this case, the formed structure of the nanowires resembles a sponge or foam with an average density ten times less than a solid one, and the thickness of a layer of such a foam can reach several millimetres. This allows it to be used for volumetric absorption of relativistic laser radiation [136, 210]. At the same time, such structures have low thermal conductivity and high brittleness, which complicates laser-plasma experiments at a high pulse repetition rate and imposes very stringent requirements on the contrast of a laser pulse [54].

Over the last decade, 3D microprinting and laser micromachining technologies have been developed [244, 245]. With this approach, the possible variations in the morphology of structures become by and large countless, and they very quickly found application in laser-plasma research [220, 246, 247].

Ordinary optical diffraction gratings can be classified as a separate type of targets with a structured surface. They have a high homogeneity over the entire sample area and a period varying over a wide range of values, but have a rela-

tively small aspect ratio (close to unity) and represent a one-dimensional structure, which also determines the features of particle acceleration in laser-plasma experiments [196, 248, 249]. We also note the possibility of fabricating periodic structures of the diffraction grating type on the target surface during laser ablation [192, 219].

Finally, one of the most exotic types of structures that have been successfully applied in plasma experiments is the living environment. Thus, a number of studies [198, 250] show the promise of using a layer of *Escherichia coli* on a solid substrate. In general, the use of biotargets can have a rather interesting further development due to the high variability of the forms of living objects.

6.2. Surface structuring for producing an X-ray source

When designing a laser-plasma X-ray source, the determining role is played by the spatial coherence of the source (for obtaining high-resolution images, including by phase contrast methods) and luminosity per unit time. Therefore, much attention in these studies is paid to targets with a large area capable of operating at a high pulse repetition rate. In this case, there is no need to chase the record energies of charged particles, but it is necessary to increase their flux. In part, this also applies to the parameters of the laser pulse itself. Too high pulse energy or pulse intensity leads to an increase in the transverse dimensions of the hot plasma and, as a consequence, to deterioration of spatial coherence.

One of the first works is paper [195], in which, in addition to the experimental observation of the effect of an increase in the yield of hard X-ray radiation in the range from 10 to 100 keV, a theoretical explanation was also proposed. The authors attributed the twofold increase in the temperature of hot electrons in the plasma of nanoparticles deposited on a substrate [251] not only with increased absorption, but also with the effect of amplification of the local field (lightning rod). A relatively simple model was proposed for estimating the effective field near inhomogeneities, which found application in the works of other authors, for example, using copper nanorods [207], silicon nanowires [235], carbon nanotubes [252], and suspension of gold nanoparticles [253]. This indicates the broad applicability of this model for evaluating the efficiency of electron acceleration in plasma. Note that we are not talking about the accumulation of energy by particles due to the action of a new acceleration mechanism. It is often assumed (at least at intensities up to 10^{18} W cm^{-2}) that the main mechanism of energy gain is the effect of vacuum heating (the Brunel effect, see, for example, [254]) or resonant absorption (see, for example, [207]) at a rather sharp plasma–vacuum boundary, which, of course, presupposes the use of a pulse with a high contrast (but already at high intensities [235]). In addition, the developed three-dimensional surface of the structured target becomes a significant factor, which ensures an increase in both the number of accelerated electrons and their average energy due to multiple interactions of electrons with the surface [202].

An increase in absorption, leading to an increase in the yield of hard X-ray radiation from the plasma, was also achieved for structures with a high periodicity (diffraction gratings and ordered micro-objects) [190, 192–194]. A model describing the optimal grating parameters at which

effective acceleration of electrons is achieved in a complex combination of an electrostatic field near inhomogeneities and a laser field was proposed in [255].

When the intensity is increased to the relativistic threshold (several units per 10^{18} W cm^{-2}), the use of targets with a complex surface structure is also beneficial from the point of view of increasing the brightness of the laser-plasma X-ray source. Nevertheless, the requirements for the contrast of the laser pulse are obviously becoming more rigorous. For example, in [50], where the authors studied the interaction of a laser pulse of near-relativistic intensity ($K_{ASE} \sim 4 \times 10^{-8}$) with an array of silicon nano-rods, it is noted that the structures give a significant increase in the yield of X-ray radiation at an intensity of $(3-4) \times 10^{17}$ W cm^{-2}, while at $I = 10^{18}$ W cm^{-2} the ASE pedestal destroys the structures. However, what is most interesting, the authors, based on the observation of the generation of the three-half harmonic (clear evidence of an extended pre-plasma and parametric processes in it [68]), make a fair conclusion that a reduced threshold of plasma formation on structures leads to the formation of a more extended pre-plasma than in case with a flat target. And the processes of gaining energy by electrons, which are characteristic of a diffused target boundary, are already more efficient in such a target. It is all the more surprising that one can still find works that report a significant increase in the X-ray yield upon irradiation of nanostructured [256] or porous targets [257] with a relativistic pulse ($I > 10^{18}$ W cm^{-2}) with $K_{ASE} \sim 10^{-5}$ and in which the authors emphasise precisely the interaction with structures, and not with the inevitably formed extended pre-plasma. The value of contrast is also not given in paper [258]. Its authors claim the effects of strengthening the local field on nanoscale bacteria, leading to a multiple increase in the output of bremsstrahlung gamma radiation (peak intensity up to 3×10^{18} W cm^{-2}).

There are relatively few experimental studies on the irradiation of solid-state structured targets with $I \sim 10^{18}$ W cm^{-2}, which is explained by several reasons. First, these are the lowered thresholds for ablation and melting of such targets. Secondly, these are the complexity of operation in a multi-pulse regime and, accordingly, data accumulation – at high intensity, a solid-state target begins to heavily contaminate the vacuum interaction chamber and optics. This is a problem even for a laser operating at a pulse repetition rate of 10 Hz. Finally, for really high-power laser systems (hundreds of TW and more), there is a natural desire to work at high intensities (over 10^{19} W cm^{-2}), although already in the single-pulse regime.

Nevertheless, among the published works, there are also those where the emphasis is placed on the pulse contrast, and its value allows one to admit the preservation of nanostructures in one form or another by the time of the arrival of the peak of the main pulse. Samsonova et al. [259] discuss the efficiency of the generation of K_α lines of zinc (~ 9 keV) in a target made of zinc oxide nanorods. A conversion factor of $\sim 10^{-4}$ to a linear component was achieved (pulse energy 0.8 J, irradiation at the second harmonic frequency with $K_{ASE} < 10^{-9}$, peak intensity exceeding 10^{19} W cm^{-2}).

Investigations of the generation of gamma radiation (with an energy of more than several hundred keV) were carried out using micro- [239] and nanostructured targets [235]. An order of magnitude increase was achieved in the

conversion efficiency to energies above 300 keV when using silicon nanograss as compared to using a smooth substrate. The contrast of the laser pulse in the experiments was further improved by the XPW system to $K_{ASE} < 10^{-9}$.

The efficiency of conversion of the energy of a laser pulse into a flux of hard X-ray quanta strongly depends on the considered energy range of these quanta, but in most cases does not exceed 0.001%–0.01%. The use of structured targets makes it possible to increase the brightness of the source by one or two orders of magnitude [191, 194, 195]. In this case, the brightness of the X-ray bremsstrahlung source also depends on the target material (more precisely, on its atomic number). Silicon, traditionally used to produce structured targets, from this point of view, is very inferior to heavy metals; therefore, an important task is to fabricate targets using substances such as tungsten, tantalum, lead, and others. At the same time, for such targets, the contrast should be even higher than for silicon.

Operation at a relatively low intensity, up to 10^{19} W cm^{-2} (by the standards of modern systems with a power of up to units of PW), does not allow the brightness of the source to be dramatically increased due to the fact that hard X-ray radiation is generated by scattering on ions and atoms of hot electrons, the concentration of which is relatively low. The main part of the energy is carried away during the hydrodynamic expansion of the plasma.

This problem was solved and the regime of dominance of radiation energy losses by plasma over hydrodynamic losses was realised by irradiating ordered metal nanorods with a high-power pulse [260]. In such a system, radiation is capable of penetrating to a depth of several micrometres, that is, much deeper than the skin layer, pushing electrons towards the substrate. Fast electrons heated by a pulse of relativistic intensity (4×10^{19} W cm^{-2}), as well as reverse currents in the columns, lead to their very rapid expansion in the transverse direction with the formation of a plasma of almost solid-state density. A temperature of the order of 10 keV and a high collision frequency contribute to an efficient loss of energy through the X-ray generation channel (linear, bremsstrahlung, etc.). The measured conversion factor of the energy of a laser pulse into an ultrashort (about 1 ps) X-ray pulse with an energy of a few keV was about 20%, which is a record value today. High contrast of radiation is critical in such experiments. By doubling the frequency of the main pulse, the authors managed to achieve $K_{ps} < 10^{-12}$.

Another method for generating X-rays (but with a higher energy – up to 100 keV) using a pulse of relativistic intensity ($\sim 10^{19}$ W cm^{-2}) and a target of nanorods was proposed (numerically) in [261]. The idea is to generate synchrotron radiation by electrons accelerated in a wake wave to energies of several hundred MeV. The role of an undulator is played by nanorods ionised by a laser pulse (the same that preliminarily accelerated the electrons) (about 100 nm in diameter and tens of micrometres in length), located perpendicular to the beam in a checkerboard pattern (the distance between the columns is 5.5 μm). The fast electrons leave the rods, but during the flight of the pulse, the ions are still cold. As a result, a quasi-static field is formed around the columns, which deflects electrons from the wake beam. Correctly selected period of arrangement of the columns and the field around

them determine the parameters of the undulator and, as a consequence, the characteristics of synchrotron radiation. The authors predict that in this way it is possible to generate more than 10^7 photons by an electron beam with a charge of 50 pC.

Fundamentally new possibilities open up in the ultrarelativistic regime of interaction (that is, at $I > 10^{20}$ W cm^{-2}), when radiation effects turn out to be significant. Thus, in the ultrarelativistic regime, when the dynamics of an electron in the laser field becomes highly nonlinear, the generation of gamma quanta is possible as a result of synchrotron radiation by electrons at the kinks of the trajectories. Here again, structured targets have an advantage over flat targets. Thus, for a normal incidence of a pulse with an intensity above 10^{22} W cm^{-2} on a periodic ribbed surface with a period of less than 1 μm, a height and width of a rectangular tooth of less than 0.5 μm, a several-fold increase in the yield of gamma quanta was numerically demonstrated in [262]. The authors attribute this to increased absorption, complex electron trajectories and their increased energy in comparison with the case of using a flat foil.

In [227], the propagation of a laser pulse ($I > 10^{22}$ W cm^{-2}) between nanorods about 10 μm in length was considered. It was shown that, under the action of laser radiation, electrons ejected from the surface of the rods are accelerated along them by a field in the form of bunches with an energy of several hundred MeV, which also emit synchrotron radiation of similar energy at the kinks of the trajectories. Gamma quanta form ultrashort (~300 as) well-collimated bunches that can be used for problems of ultrafast diagnostics of matter.

Of considerable interest is the use of recently appeared high-power mid-IR lasers in experiments with structured targets. This is due, first of all, to the quadratic dependence of the oscillatory energy of electrons on the wavelength, that is, the transition to the relativistic regime of interaction is possible at lower intensities than in the optical and near-IR ranges. In addition, an important circumstance is an increase in the threshold intensities for ionisation [263] and ablation [264] with increasing wavelength, which also weakens the requirements for the contrast of laser radiation. The possibility of developing an X-ray laser-plasma source was demonstrated in [265], and in [266], the results of experiments with arrays of silicon nanowires at a laser wavelength of 3.9 μm were presented for the first time.

In addition to bremsstrahlung X-ray radiation, betatron radiation can also be generated in a plasma during direct laser acceleration in the plasma channel [267, 268]. Under certain conditions, when an array of parallel nanorods is irradiated, betatron resonance with an external laser field can be achieved. Lécz and Andreev [269] showed that with an optimal ratio between the column diameter, electron density and laser radiation intensity (~10^{20} W cm^{-2}), electrons, rotating around and moving along the rod under the action of electric and magnetic fields, emit intense synchrotron radiation with energies above 1 keV at a laser pulse intensity of 6×10^{19} W cm^{-2}. A strongly nonlinear (power law with an exponent of 5/2) growth of the flux of X-ray quanta with an increase in the intensity of laser radiation was also predicted.

6.3. Micro- and nanostructured targets for accelerating charged particles

Of interest for applications are also beams of charged particles (electrons or ions) with a sufficiently high energy (for electrons, more than units of MeV), obtained in the relativistic regime of interaction. The physics of the process of energy gain in the relativistic regime becomes more complicated and cannot be described within the framework of simple models. Below, we will try to discuss some of the key phenomena. Note also that in the regime of interaction with structured targets in question, the laser radiation contrast, as a rule, should be as high as possible to prevent the spreading of structures under the action of pre-pulses of various nature. Thus, for the recently discussed intensities of 10^{21} W cm^{-2} and higher, a contrast better than 10^{-12} is required both in ASE and in short pre-pulses. The effect of the contrast of relativistic laser radiation during its interaction with various structures (obtained by electrochemical etching and deposition) was studied in [54]. In particular, the thresholds of plasma formation under the action of pre-pulses were experimentally estimated for such structures.

With an increase in the amplitude of the incident laser field, the oscillatory and ponderomotive energies of the electron increase as well. In this case, in the presence of submicron structures in the interaction region, electrons at different moments of their motion can be both outside and inside dense structures that are nontransparent to laser radiation. If a particle spend a long enough time outside the laser field, then it can return into another phase of this field. In this case, a relationship appears between the intensity of the incident pulse and the characteristic size of the structures: The time of flight of an electron through a separate element of the structure should be approximately equal to half the period of the field or longer for it to return in the accelerating phase. In this case, amplification of the local field at the inhomogeneities is absent as such; a significant increase in energy is achieved only due to prolonged exposure of the electron to the required phase of the accelerating field. This stochastic multistage process of energy gain was discussed for cluster targets [270], studied numerically in sufficient detail for structures of various shapes and sizes [224, 227], and also observed experimentally [235, 271]. In this context, we should briefly mention the interesting concept [247, 272] of obtaining high-strength fields, for example, for additional acceleration of particle beams from an accelerator. According to this idea, with the simultaneous propagation of a relativistic electron beam across a periodic structure (lattice) and its irradiation with a laser pulse, it is possible to achieve phase matching conditions when electrons will experience only an accelerating field passing through the lattice gaps, and the phase of the decelerating field will fall on the moment the particle is located inside a volume with supercritical density. However, this phenomenon has not yet been realised experimentally.

New regimes of electron acceleration are possible using volumetric low-density targets that are transparent to a relativistic laser pulse. In this regime, nanostructures are essential. The idea is that the average density of electrons

in the produced plasma should be slightly less than the critical one (taking into account the effect of relativistic transparency, that is, a decrease in the plasma frequency due to the relativistic change in the electron mass in a strong laser field [273]). For targets made of light atoms, this corresponds to the density of the initial substance in thousandths of a gram per cm^3, that is, substantially less than the solid-state density. Low-density quasi-homogeneous substances such as aerogels do not satisfy this criterion. When they are ionised by a laser field, a plasma with a too high supercritical electron density is formed, while targets such as a gas jet, on the contrary, as a rule, have a significantly lower density. In this case, a nanostructured foam with the desired density can be fabricated by using modern technologies [136, 274]. The foam, already at the front of the propagating laser pulse, can be transformed into a quasi-homogeneous plasma (due to field ionisation) with an electron density close to, but less than, the critical one. Numerical calculations show that this medium is optimal for implementing direct laser acceleration of electrons and obtaining electron beams with charges up to 100 pC [136, 267]. The key role of nanostructures was confirmed for both gas-cluster jets [275] and foams [210]. In particular, in Ref. [210], a threefold increase in the energy absorption by electrons was found in comparison with the case of a homogeneous low-density medium.

Structured targets can also be used to generate beams of accelerated ions. For example, effective ion acceleration is possible by irradiating an ordered array of nanorods with a laser pulse having an intensity of $\sim 10^{20}$ W cm^{-2} [276]. A rapid escape of electrons from the nanorods under the action of the laser field makes these nanorods transparent to optical radiation, resulting in the formation of a kind of a waveguide, where ions gain energy more efficiently (up to 8 MeV). In the presence of a pre-plasma, the effectiveness of such a process is significantly reduced.

Structured targets can also be used to optimise the ion acceleration process in the standard TNSA scheme. This optimisation concerns, first of all, the improvement of the collimation of the ion beam (suppression of edge effects, amplification of the ambipolar field). A number of concepts have been proposed based on micromodification of the rear surface of the target. For example, Kawata et al. [277] proposed a target with periodic submicron-sized holes for a more directed acceleration of protons. They found numerically that electrons exposed to a high-power laser pulse are accelerated along the walls of the holes, forming a strong azimuthal magnetic field. The authors of this work reported an increase in the collimation of the proton beam in comparison with a flat target and an increase in energy up to 200–250 MeV, sufficient for proton therapy of oncological diseases. To obtain protons with an energy of ~ 60 MeV at $I = 10^{20}$ W cm^{-2}, Fazeli [225] proposed to place a thin hydrogen-saturated washer on the rear side of the carbon film, the diameter of which is smaller than the diameter of the laser beam waist. The protons accelerated from the washer are in this case in a more uniform field of electrons, and heavier ions from the depth of the target produce a focusing effect due to their greater charge.

It should be noted that, when structuring the rear side of the target, the requirements for contrast are similar to those imposed upon ion acceleration on flat foils in the TNSA regime. In this case, structuring can also be carried

out on the front side of the target. Nevertheless, in the works devoted to the acceleration of protons, one can find ambiguous conclusions, supported by simulations, about the favourable effect of nanoparticles on the front side of the target with the declared $K_{\mathrm{ASE}} < 10^{-6}$ and peak intensity above 10^{19} W cm^{-2} [278] (when all talks of the preservation of particles at the time of the arrival of the pulse peak are very conditional).

We also note a promising numerically substantiated scheme in [279], where it is proposed to form a target in the form of a thin plasma, the transverse profile of which repeats the profile of the laser pulse intensity. At an intensity of $\sim 10^{22}$ W cm^{-2}, electrons almost instantly leave the target – a thin foil, making it transparent to laser radiation and forming an almost uniform 'washer' flying in space. Calculations show that in this scheme it is possible to achieve collimation and monochromatisation of the ion flux with energies up to 1 GeV.

Finally, a quaint solution was proposed by Xiao et al. [246], who condirerd a target in the form of a microfunnel, in the narrowest part of which there is a foil (according to the authors, such a structure is easy to implement on a modern 3D printer). Propagation of a laser pulse of relativistic intensity along the funnel leads to the acceleration of electrons along its walls (an increase in the electron energy from 4 to 50 MeV is predicted in comparison with the case of a flat foil). Therefore, a large number of high-energy electrons penetrate through the foil at the rear side of the funnel, effectively accelerating the ions from the back of the foil. Similar results were obtained numerically in [280], where the authors propose to focus radiation up to $I \sim 10^{20}$ W cm^{-2} into a microwell, the walls of which are made of heavy metal (gold) with a CH foil located at the bottom. The laser pulse will rip electrons from the walls of the well and accelerate them towards the bottom. If the size of the well is optimal, then the electrons will focus on the foil and, therefore, form an amplified field that accelerates protons to 50 MeV, which is 10 times more than in the case of focusing on a flat foil.

Experimentally, Gaillard et al. [228] and Kaymak et al. [281] succeeded in observing an increase in the maximum proton energy at a laser radiation intensity above 10^{20} W cm^{-2}. In [228], irradiated was a target in the form of a hollow truncated cone with a wall thickness of the order of several micrometres and a radius significantly larger than the diameter of the laser beam waist, and in [281], it was a hemisphere of an ultrathin (~ 100 nm) film with a radius of ~ 10 μm. In both works, the authors explain the observed result by the action of the hybrid mechanism of energy gain by electrons – the so-called direct laser light pressure acceleration. When a pulse is incident on a curved surface near it, the incident and reflected waves interfere, and in this interference field the electrons gain a speed close to that of light. An additional charge separation field, as well as the direct action of light with a force $v \times B$, lead to the appearance of electron beams moving through the target and accelerating the ions. In [228], due to the large thickness of the cone walls, the ion acceleration regime refers to TNSA [the authors increased the maximum proton energy from 55 MeV (for a flat target) to almost 68 MeV]. In [281], where the substrate thickness was very small, the ion energy gain regime was more likely

to be radiation pressure acceleration (RPA [282]), which explained the rather low ($\sim$8.5 MeV) maximum proton energy for a structured target ($\sim$5 MeV for flat). However, the RPA mechanism has a higher power-law dependence of the proton energy on the laser radiation intensity, which makes it promising in the ultrarelativistic interaction regime.

If we discuss the case when several neighbouring structures are located the waist region at once, then the effects of increased absorption of radiation and, of course, the size and shape of the structures begin to play a role. The role of the shape of microstructures on the front side of the target was studied in [283]. It is shown that the optimal size is about half the wavelength. The authors numerically obtained almost 100% absorption of radiation and an increase in the proton temperature from 0.4 to 1.6 MeV at $I \sim 3.5 \times 10^{19}$ W cm^{-2}.

Recently, there have appeared proposals on the possibility of using double-layer targets for accelerating ions, for example, a low-density foam deposited on a solid-state film. In this case, the front layer acts as an effective absorber of laser radiation. Fideli et al. [284] numerically studied the effect of the morphology of such a foam and showed that not only its density, but also its spatial structure is important. For example, a foam consisting of nanorods/nanofibers has been shown to be more effective than a homogeneous foam generated by random nanoclusters and nanopores. Experimentally, the positive effect of an ultra-low-density layer of carbon nanotubes in front of a thin dense film was demonstrated in [285]: A multiple increase in the number of fast protons and an increase in their maximum energy from 10 to 30 MeV at a peak intensity of $\sim 10^{20}$ W cm^{-2} were discovered. In another version of a two-layer target, a layer of gold nanoparticles was used to increase the absorption of laser radiation [236].

6.4. Nuclear physics, high energy physics and quantum electrodynamic effects in laser-plasma experiments using structured targets

To date, a number of interesting numerical and experimental results in related and applied research areas have been demonstrated using structured targets. All these data were obtained for pulses with a high radiation contrast, providing direct interaction with structures unperturbed by a pre-pulse.

First of all, we are refering to an increase in the efficiency of a thermonuclear reaction. The first neutrons under irradiation of deuterated structured titanium were detected already at $I = 10^{16}$ W cm^{-2} almost 20 years ago [143].

A series of studies on the effect of high-contrast relativistic laser radiation on an array of nanorods has been published over the past several years [260, 286, 287]. The authors have shown numerically and experimentally that with the penetration of radiation between the nanorods, their subsequent rapid heating and expansion, a very high energy density (up to GJ cm^{-3}) and a temperature of several keV are achieved along with a high ionisation rate (up to 52 for gold). At the same time, the electron pressure in the plasma almost reaches 1 TBar, which is comparable to the pressure during compression of the capsule in experiments on the NIF setup [288]. In this case, fast electrons gain an energy of several MeV, further accelerating the ions. This set of parameters opens up the possibility of efficient initiation of nuclear fusion reactions with the generation of neutrons. A record neutron flux, over 10^6 neutrons per 1 J of laser energy, was achieved under irradiation of nanorods made of deuterated polyethylene as a result of the DD-n reaction [289]. This flux is two orders of magnitude more the one obtained using a flat target.

Optimisation of the acceleration of deuterium ions with foam targets was considered in Ref. [290]. Fast electrons leaving the interfaces inside the foam form a strong field that accelerates the ions inside the target. Numerical simulations showed an increase in the deuteron energy up to 100 MeV and more at $I \sim 10^{21}$ W cm^{-2}. Foamed targets are also of significant interest for thermonuclear fusion in the fast ignition scenario [291].

A twofold increase in the efficiency of the fusion reaction was observed experimentally in [292] when a high-contrast femtosecond pulse with $I = 2 \times 10^{18}$ W cm^{-2} was applied to low-density (less than 0.4 g cm^{-3}) deuterated polyethylene. The peak value of the neutron flux was estimated at 10^5 per 1 J of laser energy. The observed effect is explained by an increase in the efficiency of absorption of the laser energy. In experiments with a picosecond laser with a peak intensity of $\sim 10^{16}$ W cm^{-2} and using a similar target, but with a lower density, the optimal foam density was found to be $1-3$ mg cm^{-3} with a maximum neutron yield of $\sim 7 \times 10^5$ per 1 J of laser energy [293]. Studies with foamed targets were also carried out with a low contrast pulse ($K_{ASE} \sim 10^{-4}$) [294]. The authors did not observe an increase in the neutron yield, which clearly indicates the role of high contrast in the irradiation of low-density targets.

Finally, the developemtn of multipetawatt laser systems in the near future spurs interest in the study of the phenomena of quantum electrodynamics, including the use of a combination of such lasers and structured targets. One of these effects is the production of electron–positron pairs. There are a lot of works considering laser concepts of this phenomenon (see papers [295–297] and references therein), but for structured targets we are talking about the Breit–Wheeler process of scattering of a gamma quantum by optical photons [298, 299]. The idea is based on the generation of high-energy electron beams with an energy of $\sim$1 GeV during the propagation of an ultrarelativistic ($I = 10^{23}$ W cm^{-2}) laser pulse along a single nanorod [300] or their array [227]. Next, a beam of gamma quanta is formed. In one case, this is the process of generating directional synchrotron radiation [227] with a photon energy of hundreds of MeV. Li et al. [300] proposed to collide beams of electrons with a counterpropagating laser pulse and generate gamma quanta with an energy of 24 MeV due to the inverse Compton effect. For the production of positrons, in any case, the presence of a laser field is necessary. In [227], it was proposed to place a reflecting foil behind an array of nanorods, and in [300], the same counterpropagating laser pulse will act as a source of photons. It is important to note that the temporal pattern of positron beams repeats the pattern for gamma quanta, and the latter is directly related to the characteristics of the electron beams. In both cases, the electrons form a sequence of attosecond pulses, which means that the positron pulses have a comparable duration. The energy density in positron beams reaches 10^{17} J m^{-3}, and the total number of particles exceeds 10^{10}, which makes them interesting for

various applications related to high energy density physics.

7. Conclusions

Thus, the processes occurring during the interaction of a relativistically intense femtosecond laser pulse with dense targets are largely determined by the parameters of the pre-plasma layer, the formation of which is very difficult to avoid. Neglecting the presence of this layer when simulating and interpreting experimental results can lead to incorrect conclusions and unreliable estimates. The pre-plasma layer is formed as a result of the action of various types of pre-pulses on the target, which are inevitably present in the temporal structure of radiation of all types of laser systems generating ultrashort optical pulses. These are short (femtosecond) pre-pulses ahead of the main pulse by tens to hundreds of picoseconds or by several nanoseconds; amplified spontaneous emission of nanosecond duration; short pre-pulses with a lead time of $0.1 - 5$ ps. To characterise all these pre-pulses, it is necessary to measure the contrast by the intensity for each of them, which is a rather laborious task. In most cases, ASE would be the most crucial parameter, which, even with good contrast, has a significant energy density on the target.

It is important to emphasise that the presence of a pre-plasma layer is not necessarily a negative factor. In particular, as shown in this review, in a number of cases it is the pre-plasma layer with optimised parameters that provides efficient generation of directed beams of relativistic electrons with a large specific charge per unit of input energy.

Since the transfer of energy from a laser pulse to a plasma occurs mainly in the range of electron densities from 0.1 to 0.5 of the critical value, for the problems discussed in this review, the key parameter is not the maximum or average density, but the density gradient in this plasma region. In the case of a smooth density gradient, $L \gg \lambda$, both self-focusing of the beam and its ionisation defocusing can occur in a rarefied plasma; in the case of $L \sim \lambda$, the absorption of radiation becomes significant due to the excitation of waves of parametric instabilities; and at sharper gradients – due to nonlinear resonance absorption, vacuum heating, etc. An additional artificial pre-pulse can be used to control the gradient parameters. This provides more reliable control, since it allows one to independently change the energy, duration and intensity of the pre-pulse on the target.

The most efficient acceleration and heating of electrons to relativistic energies occurs in the region $n_{\mathrm{e}} = (0.1-1)n_{\mathrm{cr}}$ as a result of the excitation of plasma waves caused primarily by parametric instabilities in the region $n_{\mathrm{e}} = n_{\mathrm{cr}}/4$ [134, 301]. These instabilities do not develop both in the case of $L/\lambda > 10$ and for too sharp gradients, $L/\lambda < 1$. Optimisation of such an acceleration regime and heating of electrons is associated with the selection of the parameters of the artificial pre-pulse and/or ASE, as well as the duration of the laser pulse, its intensity, etc. Under certain conditions, plasma waves excited through parametric instabilities can serve as an injector for acceleration in a rarefied plasma by the direct laser acceleration mechanism. This approach makes it possible to obtain well collimated $(20-50$ mrad$)$ beams of relativistic electrons with an average energy of up to tens of MeV and a specific charge of up to 1 nC per 1 J of laser energy. For a wide range of applied problems, such a source of electrons may turn out to be preferable to a source based on acceleration in a gas jet by the LWFA mechanism.

Laser acceleration of ions in plasma, as a rule, implies the presence of extremely sharp electron density gradients and the use of ultrathin film targets, which dictates the need for the highest possible contrast of radiation at all time scales and, moreover, additional sharpening of the leading edge of the laser pulse using the plasma mirror technology. Pre-pulses and ASE can clean the surface of thick targets and increase the efficiency of acceleration of multiply charged ions. On films with a thickness of $1-10$ μm, pre-pulses blur the border on the rear surface, reducing the acceleration efficiency. At the same time, the regime of ion acceleration in a dense, almost critical, plasma is also considered, which can provide a significant increase in the the ion beam charge.

Targets with a structured surface should be addressed separately from the point of view of the effect of the contrast of laser radiation. Here, a necessary condition for an increase in the absorption of laser radiation energy, the energy and number of electrons and the efficiency of ion acceleration is also the use of high-contrast laser pulses to prevent the spreading of structures prior to interaction with the main laser pulse. In this case, the thresholds for destruction of nanostructures and microstructures are lower than for a smooth surface. As an alternative approach one can consider the experiments, in which the complete destruction of structures on the surface or in the volume ensures the formation of a layer of quasi-homogeneous plasma with the desired average density of electrons (usually subcritical) by the time of exposure to the main laser pulse.

In the near future, laser systems with a high, kilohertz, pulse repetition rate and peak power of $10-100$ TW will become available and widespread. With that one should expect the emergence of effective laboratory sources of electrons, gamma radiation and secondary particles for solving various fundamental and applied problems. Optimisation of these sources is inevitably associated with pre-plasma optimisation, as well as with the use of structured targets and other approaches discussed above.

References

1. Yoon J.W. et al. *Opt. Express*, **27** (15), 20412 (2019).
2. Jourdain N. et al. *Matter Radiat. Extrem.*, **6** (1), 015401 (2021).
3. Gales S. et al. *Rep. Prog. Phys.*, **81** (9), 94301 (2018).
4. Umstadter D. *J. Phys. D: Appl. Phys.*, **36** (8), R151 (2003).

5. Gibbon P. *Short Pulse Laser Interaction with Matter: An Introduction* (London: Imperial College Press, 2005).

6. Daido H., Nishiuchi M., Pirozhkov A.S. *Rep. Prog. Phys.*, **75** (5), 056401 (2012).

7. Macchi A., Borghesi M., Passoni M. *Rev. Mod. Phys.*, **85** (2), 751 (2013).

8. Carr G.L. et al. *Nature*, **420** (6912), 153 (2002).

9. Mun J. et al. *J. Korean Phys. Soc.*, **51** (91), 421 (2007).

10. Albert F., Thomas A.G.R. *Plasma Phys. Controlled Fusion*, **58** (10), 103001 (2016).

11. Nedorezov V.G., Savel'ev-Trofimov A.B. *Phys. At. Nucl.*, **80** (9), 1477 (2017) [*Yad. Fiz.*, **7** (6), 479 (2016)].

12. Higginson D.P. et al. *Phys. Plasmas*, **17** (10), 100701 (2010).

13. Gorlova D.A., Nedorezov V.G., Ivanov K.A., Savel'ev A.B., Turinge A.A., Tsymbalov I.N. *Quantum Electron.*, **47** (6), 522 (2017) [*Kvantovaya Elektron.*, **47** (6), 522 (2017)].

14. Liu J.X. et al. *Phys. Plasmas*, **22** (10), 103102 (2015).

15. Esarey E., Schroeder C.B., Leemans W.P. *Rev. Mod. Phys.*, **81** (3), 1229 (2009).

16. Goers A.J. et al. *Phys. Rev. Lett.*, **115** (19), 194802 (2015).

17. Ledingham K.W.D., Galster W. *New J. Phys.*,**12** (4), 045005 (2010).

18. Rousse A. et al. *Phys. Rev. Lett.*, **93** (13), 135005 (2004).

19. Döpp A. et al. *Optica*, **5** (2), 199 (2018).

20. Hazra D. et al. *Plasma Phys. Controlled Fusion*, **60** (8), 85015 (2018).

21. Belyaev V.S. et al. *Laser Phys.*, **27** (6), 066001 (2017).

22. Thos A. PhD Thesis (Berlin, Freien Univ., 2003).

23. Perry M.D. et al. *Rev. Sci. Instrum.*, **70** (1), 265 (1999).

24. Liesfeld B. et al. *Appl. Phys. B*, **79** (8), 1047 (2004).

25. Najmudin Z. et al. *Philos. Trans. A Math. Phys. Eng. Sci.*, **372** (2010), 20130032 (2014).

26. Gonsalves A.J. et al. *Phys. Rev. Lett.*, **122** (8), 84801 (2019).

27. Couperus J.P. et al. *Nat. Commun.*, **8** (1), 487 (2017).

28. Mordovanakis A.G. et al. *Phys. Rev. Lett.*, **103** (23), 235001 (2009).

29. Chopineau L. et al. *Phys. Rev. X*, **9** (1), 011050 (2019).

30. Li Y.T. et al. *Phys. Rev. E*, **64** (4), 046407 (2001).

31. Maine P. et al. *IEEE J. Quantum Electron.*, **24** (2), 398 (1988).

32. Bromage J. et al. *High Power Laser Sci. Eng.*, **7**, e4 (2019).

33. Kalashnikov M., Osvay K., Sandner W. *Laser Part. Beams*, **25** (2), 219 (2007).

34. Thaury C. et al. *Nat. Phys.*, **3** (6), 424 (2007).

35. Bock S. et al. *Crystals*, **10** (9), 1 (2020).

36. Wagner F. et al. *Appl. Phys. B*, **116** (2), 429 (2014).

37. Ivanov K.A. et al. *Phys. Plasmas*, **21** (9), 093110 (2014).

38. Bolshakov V.V., Vorob'ev A.A., Uryupina D.S., Ivanov K.A., Morshedian N., Volkov R.V., Savel'ev A.B. *Quantum Electron.*, **39** (7), 669 (2009) [*Kvantovaya Elektron.*, **39** (7), 669 (2009)].

39. Hong K.H. et al. *Appl. Phys. B*, **81** (4), 447 (2005).

40. Li Z. et al. *Opt. Express*, **25** (18), 21201 (2017).

41. Didenko N.V., Konyashchenko A.V., Lutsenko A.P., Tenyakov S.Y. *Opt. Express*, **16** (5), 3178 (2008).

42. Schimpf D.N., Seise E., Limpert J., Tünnermann A. *Opt. Express*, **16** (14), 16664 (2008).

43. Khodakovskiy N. et al. *Opt. Lett.*, **41** (19), 4441 (2016).

44. Keppler S. et al. *Laser Photonics Rev.*, **10** (2), 264 (2016).

45. Gamaly E.G., Rode A.V., Luther-Davies B., Tikhonchuk V.T. *Phys. Plasmas*, **9** (3), 949 (2002).

46. Key M.H. et al. *Phys. Plasmas*, **5** (5), 1966 (1998).

47. Wagner F., Bedacht S., Ortner A., et al. *Opt. Express*, **22** (24), 29505 (2014).

48. Kalashnikov M.P. et al. *AIP Conf. Proc.*, **1462**, 108 (2012).

49. Yefet S., Pe'er A. *Appl. Sci.*, **3** (4), 694 (2013).

50. Cristoforetti G. et al. *Plasma Phys. Controlled Fusion*, **56** (9), 095001 (2014).

51. Rajeev P.P. et al. *J. Phys. IV*, **133**, 533 (2006).

52. Nishikawa T. et al. *Appl. Phys. Lett.*, **70** (13), 1653 (1997).

53. Besozzi E. et al. *Nucl. Fusion*, **58** (3), 036019 (2018).

54. Ivanov K.A. et al. *Laser Phys. Lett.*, **17** (4), 045302 (2020).

55. Phipps C.R., Dreyfus R.W., in *Laser Ionization Mass Analysis*. Ed. by A. Vertes, R. Gijbels, F. Adams (New York: Wiley, 1993) p. 369.

56. Mulser P., Weng S.M., Liseykina T. *Phys. Plasmas*, **19** (4), 043301 (2012).

57. Ge Z.Y. et al. *Phys. Plasmas*, **20** (7), 073301 (2013).

58. Ginzburg V.L. *The Propagation of Electromagnetic Waves in Plasmas* (London: Pergamon Press, 1970; Moscow: Nauka, 1967).

59. Mulser P., Bauer D. *High Power Laser-Matter Interaction* (Berlin: Springer, 2010).

60. Kruer W.L., Estabrook K. *Phys. Fluids*, **28** (1), 430 (1985).

61. Ping Y. et al. *Phys. Rev. Lett.*, **100** (8), 085004 (2008).

62. Santala M.I.K. et al. *Phys. Rev. Lett.*, **84** (7), 1459 (2000).

63. Kruer W.L. *The Physics of Laser Plasma Interactions* (Redwood: Addison-Wesley, 1988).

64. Courtois C. et al. *Phys. Plasmas*, **16** (1), 013105 (2009).

65. Culfa O. et al. *Phys. Plasmas*, **21** (4), 043106 (2014).

66. Culfa O. et al. *Phys. Rev. E*, **93** (4), 043201 (2016).

67. Malka G. et al. *Phys. Rev. Lett.*, **79** (11), 2053 (1997).

68. Ivanov K.A. et al. *Phys. Plasmas*, **24** (6), 063109 (2017).

69. Uryupina D.S. et al. *Proc. SPIE*, **8779**, 877917 (2013).

70. Filevich J. et al. *Phys. Rev. E*, **67** (5), 056409 (2003).

71. Gizzi L.A. et al. *Laser Part. Beams*, **19** (2), 181 (2001).

72. Scott R.H.H. et al. *Phys. Plasmas*, **19** (5), 053104 (2012).

73. Krestovskikh D.A., Ivanov K.A., Tsymbalov I.N., Shulyapov S.A., Bukin V.V., Volkov R.V., Rupasov A.A., Savel'ev A.B. *Quantum Electron.*, **47** (1), 42 (2017) [*Kvantovaya Elektron.*, **47** (1), 42 (2017)].

74. Shulyapov S.A., Tsymbalov I.N., Ivanov K.A., Gospodinov G.A., Volkov R.V., Bychenkov V.Yu., Savel'ev A.B. *Quantum Electron.*, **50** (4), 335 (2020) [*Kvantovaya Elektron.*, **50** (4), 335 (2020)].

75. Filevich J. et al., in *Conf. Lasers Electro-Optics (CLEO 2000). Techn. Dig. Postconf. Ed. TOPS Vol.39* (IEEE Cat. No. 00CH37088); doi 10.1109/cleo.2000.907329.

76. Jarrott L.C. et al. *Phys. Plasmas*, **21** (3), 031211 (2014).

77. Sanyasi Rao B., Arora V., Anant Naik P., Dass Gupta P. *Phys. Plasmas*, **19** (11), 113118 (2012).

78. Gray R.J. et al. *New J. Phys.*, **16** (11), 113075 (2014).

79. Borm B., Khaghani D., Neumayer P. *Phys. Plasmas*, **26** (2), 023109 (2019).

80. Hunter J.H., London R.A. *Phys. Fluids*, **31** (10), 3102 (1988).

81. Sunahara A., Sasaki A., Nishihara K. *J. Phys. Conf. Ser.*, **112**, 042048 (2008).
82. Singh P.K. et al. *Sci. Rep.*, **5** (1), 17870 (2015).
83. Murnane M.M., Kapteyn H.C., Falcone R.W. *Phys. Rev. Lett.*, **62** (2), 155 (1989).
84. Cobble J.A. et al. *J. Appl. Phys.*, **69** (5), 3369 (1991).
85. Kyrala G.A. et al. *Appl. Phys. Lett.*, **60** (18), 2195 (1992).
86. Bolshakov et al. *JETP Lett.*, **88** (6), 360 (2008) [*Pis'ma Zh. Eksp. Teor. Fiz.*, **88** (6), 415 (2008)].
87. Bolshakov V.V., Vorobiev A.A., Volkov R.V., Savel'ev A.B. *Contrib. Plasma Phys.*, **49** (7), 568 (2009).
88. Ivanov K.A. et al. *Phys. Part. Nucl. Lett.*, **11** (1), 54 (2014).
89. Beg F.N. et al. *Phys. Plasmas*, **4** (2), 447 (1997).
90. Wilks S.C., Kruer W.L., Tabak M., Langdon A.B. *Phys. Rev. Lett.*, **69** (9), 1383 (1992).
91. Gibbon P. et al. *Appl. Phys. A*, **96** (1), 23 (2009).
92. Lu W. et al. *Phys. Rev. E*, **80** (2), 026404 (2009).
93. Romanov D.V. et al. *Phys. Rev. Lett.*, **93** (21), 215004 (2004).
94. Shulyapov S.A. et al. *J. Phys. Conf. Ser.*, **653** (1), 012007 (2015).
95. Tsymbalov I.N. et al. *2014 Int. Conf. Laser Optics* (IEEE, 2014) p. 1; doi: 10.1109/LO.2014.6886347.
96. Shulyapov S.A. et al. *J. Phys. Conf. Ser.*, **1692** (1), 1 (2020).
97. Tsymbalov I.N. et al. *2016 Int. Conf. Laser Optics* (IEEE, 2016) p. R5-4; doi: 10.1109/LO.2016.7549792.
98. Tsymbalov I.N. et al. *Phys. At. Nucl.*, **80** (3), 397 (2017) [*Yad. Fiz.*, **80** (3), 189 (2017)].
99. Dawson J.M., Tajima T. *Phys. Rev. Lett.*, **43** (4), 267 (1979).
100. Esarey E., Ting A., Sprangle P. *Rev. Mod. Plasma Phys.*, **4** (1), 57 (1989).
101. Osterhoff J. et al. *Phys. Rev. Lett.*, **101** (8), 085002 (2008).
102. Nakamura K. et al. *Phys. Plasmas*, **14** (5), 056708 (2007).
103. Li F.Y. et al. *Phys. Rev. Lett.*, **110** (13), 135002 (2013).
104. Kuznetsov S.V. *Quantum Electron.*, **48** (10), 945 (2018) [*Kvantovaya Elektron.*, **48** (10), 945 (2018)].
105. Kuznetsov S.V. *Quantum Electron.*, **50** (10), 929 (2020) [*Kvantovaya Elektron.*, **50** (10), 929 (2020)].
106. Götzfried J. et al. *Phys. Rev. X*, **10** (4), 041015 (2020).
107. Ma Y.Y. et al. *Proc. Natl. Acad. Sci. U. S. A.*, **115** (27), 6980 (2018).
108. Gibbon P. *Phys. Rev. Lett.*, **73** (5), 664 (1994).
109. Compant La Fontaine A. *J. Phys. D: Appl. Phys.*, **47** (32), 325201 (2014).
110. Wharton K.B. et al. *Phys. Rev. Lett.*, **81** (4), 822 (1998).
111. Zaïm N. et al. *Phys. Plasmas*, **26** (3), 033112 (2019).
112. Gahn C., Tsakiris G.D., Pukhov A., et al. *Phys. Rev. Lett.*, **83** (23), 772 (1999).
113. Tsymbalov I. et al. *Plasma Phys. Controlled Fusion*, **61** (7), 075016 (2019).
114. Danson C.N. et al. *High Power Laser Sci. Eng.*, **7**, e54 (2019).
115. Malkov Yu.A., Stepanov A.N., Yashunin D.A., Pugachev L.P., Levashov P.R., Andreev N.E., Andreev A.A. *Quantum Electron.*, **43** (3), 226 (2013) [*Kvantovaya Elektron.*, **43** (3), 226 (2013)].
116. Wang W. et al. *Phys. Plasmas*, **17** (2), 23108 (2010).
117. Esarey E., Sprangle P., Krall J. *Phys. Rev. E*, **52** (5), 5443 (1995).
118. Wang P.X. et al. *Appl. Phys. Lett.*, **78** (15), 2253 (2001).
119. Thévenet M. et al. *Nat. Phys.*, **12** (4), 355 (2016).
120. Lévy A. et al. *Opt. Lett.*, **32** (3), 310 (2007).
121. Li Y.T. et al. *Phys. Rev. Lett.*, **96** (16), 165003 (2006).
122. Mao J.Y. et al. *Appl. Phys. Lett.*, **106** (13), 131105 (2015).
123. Serebryakov D.A., Nerush E.N., Kostyukov I.Y. *Phys. Plasmas*, **24** (12), 123115 (2017).
124. Pukhov A., Sheng Z.M., Meyer-ter-Vehn J. *Phys. Plasmas*, **6** (7), 2847 (1999).
125. Yu W. et al. *Phys. Rev. Lett.*, **85** (3), 570 (2000).
126. Wang X., Nishikawa K., Nemoto K. *Phys. Plasmas*, **13** (8), 80702 (2006).
127. Arefiev A.V., Schollmeier M., Khudik V.N. *AIP Conf. Proc.*, **1507**, 363 (2012).
128. Peebles J. et al. *Phys. Rev. E*, **98** (5), 053202 (2018).
129. Toncian T. et al. *Matter Radiat. Extrem.*, **1** (1), 82 (2016).
130. Mandal T. et al. *Phys. Plasmas*, **26** (1), 013103 (2019).
131. Liu B. et al. *Phys. Rev. Lett.*, **110** (4), 045002 (2013).
132. Malko S. et al. *Sci. Rep.*, **9** (1), 14061 (2019).
133. Tsymbalov I. et al. *Plasma Phys. Controlled Fusion*, **63** (2), 022001 (2021).
134. Tsymbalov I., Gorlova D., Savel'ev A. *Phys. Rev. E*, **102** (6), 063206 (2020).
135. Rosmej O.N. et al. *New J. Phys.*, **21** (4), 043044 (2019).
136. Rosmej O.N. et al. *Plasma Phys. Controlled Fusion*, **62** (11), 115024 (2020).
137. Bychenkov V.Yu., Brantov A.V., Govras E.A., Kovalev V.F. *Phys. Usp.*, **58** (1), 71 (2015) [*Usp. Fiz. Nauk*, **185**, 77 (2015)].
138. Cowan T.E. et al. *Phys. Rev. Lett.*, **92** (20), 204801 (2004).
139. Scuderi V. et al. *Nucl. Instrum. Meth. Phys. Res., Sect. A*, **740**, 87 (2014).
140. Borghesi M. et al. *Phys. Plasmas*, **9** (5), 2214 (2002).
141. Nedorezov V.G., Rykovanov S.G., Savel'ev A.B. *Usp. Fiz. Nauk* (2021, accepted for publication); doi: 10.3367/UFNr.2021.03.038960.
142. Ledingham K.W.D., McKenna P., Singhal R.P. *Science*, **300** (5622), 1107 (2003).
143. Volkov R.V. et al. *JETP Lett.*, **72** (8), 401 (2000) [*Pis'ma Zh. Eksp. Teor. Fiz.*, **72** (8), 577 (2000)].
144. Hah J. et al. *Plasma Phys. Controlled Fusion*, **60** (5), 054011 (2018).
145. Borghesi M. et al. *Fusion Sci. Technol.*, **49** (3), 412 (2006).
146. Robson L. et al., in *Lasers and Nuclei*. Ed. by H. Schwoerer, B. Beleites, J. Magill (Berlin, Heidelberg: Springer, 2006) Lecture Notes in Physics, Vol. 694, p. 191.
147. Tajima T., Habs D., Yan X. *Rev. Accel. Sci. Technol.*, **2**, 201 (2009).
148. Gitomer S.J. et al. *Phys. Fluids*, **29** (8), 2679 (1986).
149. Hegelich B.M. et al. arXiv:1310.8650 (2013).
150. Kim I.J. et al. *Phys. Plasmas*, **23** (7), 070701 (2016).
151. Gurevich A.V., Pariiskaya L.V., Pitaevsky L.P. *J. Exp. Theor. Phys.*, **22** (2), 449 (1966) [*Zh. Eksp. Teor. Fiz.*, **49** (2), 647 (1965)].
152. Mora P. *Phys. Rev. Lett.*, **90** (18), 185002 (2003).
153. Wilks S.C. et al. *Phys. Plasmas*, **8** (2), 542 (2001).
154. Hegelich B.M. et al. *Nature*, **439** (7075), 441 (2006).
155. Petrov G.M. et al. *Phys. Plasmas*, **17** (10), 103111 (2010).
156. McKenna P. et al. *Phys. Rev. E*, **70** (3), 036405 (2004).
157. Volkov R.V., Golishnikov D.M., Gordienko V.M., et al. *Quantum Electron.*, **33** (11), 981 (2003) [*Kvantovaya Elektron.*, **33** (11), 981 (2003)].

158. Gordienko V.M. et al. *Appl. Phys. B*, **80** (6), 733 (2005).
159. Bagnoud V. et al. *Phys. Rev. Lett.*, **118** (25), 255003 (2017).
160. Schollmeier M. et al. *Phys. Plasmas*, **22** (4), 043116 (2015).
161. Bochkarev S.G. et al. *Phys. Plasmas*, **19** (10), 103101 (2012).
162. Shulyapov S.A., Mordvintsev I.M., Ivanov K.A., Volkov P.V., Zarubin P.I., et al. *Quantum Electron.*, **46** (5), 432 (2016) [*Kvantovaya Elektron.*, **46** (5), 432 (2016)].
163. Mckenna P. et al. *Philos. Trans. R. Soc. A*, **364** (1840), 711 (2006).
164. Mackinnon A.J. et al. *Phys. Rev. Lett.*, **88** (21), 2150061 (2002).
165. Lindau F. et al. *Phys. Rev. Lett.*, **95** (17), 175002 (2005).
166. Kaluza M. et al. *Phys. Rev. Lett.*, **93** (4), 17 (2004).
167. Fuchs J. et al. *Phys. Rev. Lett.*, **99** (1), 015002 (2007).
168. Grismayer T., Mora P. *Phys. Plasmas*, **13** (3), 032103 (2006).
169. Petrov G.M. et al. *J. Appl. Phys.*, **119** (5), 053302 (2016).
170. Fang Y. et al. *Plasma Phys. Controlled Fusion*, **58** (7), 075010 (2016).
171. Nishiuchi M. et al. *Phys. Plasmas*, **15** (5), 053104 (2008).
172. Yogo A. et al. *Phys. Rev. E*, **77** (1), 016401 (2008).
173. Roth M. et al. *Phys. Rev. Spec. Top. Accel. Beams*, **5** (6), 31 (2002).
174. Bulanov S.S. et al. *Med. Phys.*, **35** (5), 1770 (2008).
175. Carroll D.C. et al. *New J. Phys.*, **12** (4), 045020 (2010).
176. Esirkepov T., Yamagiwa M., Tajima T. *Phys. Rev. Lett.*, **96** (10), 105001 (2006).
177. Bulanov S.S. et al. *Phys. Rev. E*, **78** (2), 026412 (2008).
178. Singh P.K., Andreev A.A., Kakolee K.F., Ter-Avetisyan S. *Phys. Plasmas*, **25** (11), 113113 (2018).
179. Lécz Z., Budai J., Andreev A., Ter-Avetisyan S. *Phys. Plasmas*, **27** (1), 013105 (2020).
180. Matsukado K. et al. *Phys. Rev. Lett.*, **91** (21), 215001 (2003).
181. Utsumi T. et al. *Appl. Phys. A*, **79** (4–6), 1185 (2004).
182. Willingale L. et al. *Phys. Rev. Lett.*, **96** (24), 245002 (2006).
183. Henig A. et al. *Phys. Rev. Lett.*, **103** (4), 045002 (2009).
184. Bulanov S. et al. *Phys. Lett. A*, **299** (2–3), 240 (2002).
185. Dollar F. et al. *Phys. Rev. Lett.*, **107** (6), 065003 (2011).
186. Yin L. et al. *Phys. Plasmas*, **14** (5), 056706 (2007).
187. Henig A. et al. *Phys. Rev. Lett.*, **103** (24), 245003 (2009).
188. Chen S.N. et al. *Sci. Rep.*, **7** (1), 13505 (2017).
189. Helle M.H. et al. *Phys. Rev. Lett.*, **117** (16), 165001 (2016).
190. Murnane M.M. et al. *Appl. Phys. Lett.*, **62** (10), 1068 (1993).
191. Volkov R.V., Gordienko V.M., Dzhidzhoev M.S., Kamenev B.V., Kashkarov P.K., Ponomarev Yu.V., Savel'ev A.B., Timoshenko V.Yu., Shashkov A.A. *Quantum Electron.*, **28** (1), 1 (1998) [*Kvantovaya Elektron.*, **25** (1), 3 (1998)].
192. Volkov R.V., Golishnikov D.M., Gordienko V.M., Savel'ev A.B. *JETP Lett.*, **77** (9), 473 (2003) [*Pis'ma Zh. Eksp. Teor. Fiz.*, **77** (9), 568 (2003)].
193. Kulcsár G. et al. *Phys. Rev. Lett.*, **84** (22), 5149 (2000).
194. Gavrilov S.A. et al. *Laser Part. Beams*, **22** (3), 301 (2004).
195. Rajeev P.P. et al. *Phys. Rev. Lett.*, **90** (11), 115002 (2003).
196. Kahaly S. et al. *Phys. Rev. Lett.*, **101** (14), 145001 (2008).
197. Chakravarty U. et al. *J. Appl. Phys.*, **112** (5), 053301 (2012).
198. Krishnamurthy M. et al. *Opt. Express*, **20** (5), 5754 (2012).
199. Bagchi S. et al. *Phys. Plasmas*, **19** (3), 030703 (2012).
200. Dombi P. in *Advances in Imaging and Electron Physics*. Ed. by P. Hawkes (Elsevier, 2009) Vol. 158, p. 1; doi: 10.1016/S1076-5670(09)00006-8.
201. Habara H. et al. *Phys. Plasmas*, **23** (6), 063105 (2016).
202. Mikhailova Yu.M., Platonenko V.T., Savel'ev A.B. *Quantum Electron.*, **35** (1), 38 (2005) [*Kvantovaya Elektron.*, **35** (1), 38 (2005)].
203. Macchi A. *Phys. Plasmas*, **25** (3), 031906 (2018).
204. Sgattoni A. et al. *Plasma Phys. Controlled Fusion*, **58** (1), 014004 (2016).
205. Cristoforetti G. et al. *Plasma Phys. Controlled Fusion*, **62** (11), 114001 (2020).
206. Cao L. et al. *Phys. Plasmas*, **17** (4), 043103 (2010).
207. Mondal S. et al. *Phys. Rev. B*, **83** (3), 035408 (2011).
208. Jiang S. et al. *Phys. Rev. Lett.*, **116** (8), 85002 (2016).
209. Lednev V.N. et al. *Spectrochim. Acta, Part B*, **88**, 15 (2013).
210. Fedeli L. et al. *Sci. Rep.*, **8** (1), 3834 (2018).
211. Parker S. et al. *High Power Laser Sci. Eng.*, **6**, e47 (2018).
212. Cerchez M. et al. *High Power Laser Sci. Eng.*, **7**, e37 (2019).
213. Wang Z. et al. *Opt. Lett.*, **36** (16), 3194 (2011).
214. ELI, https://eli-laser.eu/.
215. Amplitude Laser, https://amplitude-laser.com/.
216. Ebert T. et al. *High Power Laser Sci. Eng.*, **5**, e13 (2017).
217. Nagai K., Musgrave C.S.A., Nazarov W. *Phys. Plasmas*, **25** (3), 030501 (2018).
218. Li H., Ye T., Shi L., Xie C. *J. Micromech. Microeng.*, **27** (12), 124002 (2017).
219. Vorobyev A.Y., Guo C. *Laser Photon. Rev.*, **7** (3), 385 (2013).
220. Ji L.L. et al. *Sci. Rep.*, **6** (1), 23256 (2016).
221. Jang Y. et al. *Appl. Phys. Lett.*, **102** (12), 123901 (2013).
222. Fischer J., Wegener M. *Laser Photon. Rev.*, **7** (1), 22 (2013).
223. Borisenko N.G. et al. *J. Radioanal. Nucl. Chem.*, **299** (2), 961 (2014).
224. Andreev A., Kumar N., Platonov K., Pukhov A. *Phys. Plasmas*, **18** (10), 103103 (2011).
225. Fazeli R. *Phys. Plasmas*, **25** (3), 033106 (2018).
226. Cantono G. et al. *Phys. Plasmas*, **25** (3), 031907 (2018).
227. Lécz Z., Andreev A. *Phys. Rev. E*, **99** (1), 013202 (2019).
228. Gaillard S.A. et al. *Phys. Plasmas*, **18** (5), 56710 (2011).
229. Klimo O. et al. *New J. Phys.*, **13** (5), 053028 (2011).
230. Bell A.R., Kirk J.G. *Phys. Rev. Lett.*, **101** (20), 200403 (2008).
231. Amalathas A.P., Alkaisi M.M. *Micromachines*, **10** (9), 619 (2019).
232. Jo N., Shin Y.-B. *Sci. Rep.*, **10** (1), 1024 (2020).
233. Canham L.T. *Appl. Phys. Lett.*, **57** (10), 1046 (1990).
234. Rajkumar K., Pandian R., Sankarakumar A., Rajendra Kumar R.T. *ACS Omega*, **2** (8), 4540 (2017).
235. Ivanov K.A. et al. *Appl. Phys. B*, **123** (10), 252 (2017).
236. Ebert T. et al. *Phys. Plasmas*, **27** (4), 043106 (2020).
237. Alnaser A.S., Khan S.A., Ganeev R.A., Stratakis E. *Appl. Sci.*, **9** (8), 1554 (2019).
238. Golosov E.V. et al. *Phys. Rev. B*, **83** (11), 115426 (2011).
239. Ivanov K.A. et al. *Laser Phys. Lett.*, **12** (4), 046005 (2015).

240. Lübcke A. et al. *Sci. Rep.*, **7** (1), 44030 (2017).
241. Collins G., Koleśnik M., Krstić V., Holmes J.D. *Chem. Mater.*, **22** (18), 5235 (2010).
242. Gavrilov S.A. et al. *J. Raman Spectrosc.*, **49** (5), 810 (2018).
243. Szerypo J. et al. *Matter Radiat. Extrem.*, **4** (3), 035201 (2019).
244. Hirt L. et al. *Adv. Mater.*, **28** (12), 2311 (2016).
245. Tanvir Ahmmed K.M., Grambow C., Kietzig A.M. *Micromachines*, **5** (4), 1219 (2014).
246. Xiao K.D. et al. *AIP Adv.*, **6** (1), 015303 (2016).
247. Pukhov A. et al. *Eur. Phys. J. Spec. Top.*, **223** (6), 1197 (2014).
248. Bigongiari A. PhD Thesis (Paris, Ecole Polytechnique, 2012).
249. Hu G.Y. et al. *Phys. Plasmas*, **17** (8), 083102 (2010).
250. Dalui M. et al. *Sci. Rep.*, **4** (1), 6002 (2015).
251. Ayyub P. et al. *Appl. Phys. A*, **73** (1), 67 (2001).
252. Bagchi S. et al. *Phys. Plasmas*, **18** (1), 014502 (2011).
253. Masim F.C.P. et al. *ACS Photonics*, **3** (11), 2184 (2016).
254. Ovchinnikov A.V. et al. *Laser Part. Beams*, **29** (2), 249 (2011).
255. Wang W.M., Sheng Z.M., Zhang J. *Phys. Plasmas*, **15** (3), 030702 (2008).
256. Wang H.J., Li Z.R., Chen Z. *Bin ACS Omega*, **5** (33), 20765 (2020).
257. Wang H., Li Z., Chen Z. *Appl. Phys. B*, **124** (9), 172 (2018).
258. Krishnamurthy M. et al. *Opt. Express*, **23** (14), 17909 (2015).
259. Samsonova Z. et al. *AIP Conf. Proc.*, **1811** (1), 180001 (2017).
260. Hollinger R. et al. *Optica*, **4** (11), 1344 (2017).
261. Andriyash I.A. et al. *Nat. Commun.*, **5** (1), 4736 (2014).
262. Serebryakov D.A., Volkova T.M., Nerush E.N., Kostyukov I.Y. *Plasma Phys. Controlled Fusion*, **61** (7), 074007 (2019).
263. Wu J., Guo C. *Adv. Stud. Theor. Phys.*, **2** (6), 271 (2008).
264. Sikora A., Grojo D., Sentis M. *J. Appl. Phys.*, **122** (4), 045702 (2017).
265. Weisshaupt J. et al. *Nat. Photonics*, **8** (12), 927 (2014).
266. Samsonova Z. et al. *Phys. Rev. X*, **9** (2), 021029 (2019).
267. Arefiev A.V. et al. *Phys. Plasmas*, **23** (5), 056704 (2016).
268. Huang T.W. et al. *Phys. Rev. E*, **93** (6), 063203 (2016).
269. Lécz Z., Andreev A. *Phys. Plasmas*, **24** (3), 033113 (2017).
270. Breizman B.N., Arefiev A.V., Fomyts'kyi M.V. *Phys. Plasmas*, **12** (5), 056706 (2005).
271. Andreev A. et al. *Plasma Phys. Controlled Fusion*, **58** (1), 014038 (2015).
272. Plettner T., Lu P.P., Byer R.L. *Phys. Rev. Spec. Top. Accel. Beams*, **9** (11), 111301 (2006).
273. Palaniyappan S. et al. *Nat. Phys.*, **8** (10), 763 (2012).
274. Khalenkov A.M. et al. *Laser Part. Beams*, **24** (2), 283 (2006).
275. Zhang L. et al. *Appl. Phys. Lett.*, **100** (1), 014104 (2012).
276. Dozieres M. et al. *Plasma Phys. Controlled Fusion*, **61** (6), 065016 (2019).
277. Kawata S. et al. *Laser Ther.*, **22** (2), 103 (2013).
278. Vallières S. et al. *Phys. Rev. Accel. Beams*, **22** (9), 091303 (2019).
279. Chen M., Pukhov A., Yu T.P., Sheng Z.M. *Phys. Rev. Lett.*, **103** (2), 024801 (2009).
280. Zou D.B. et al. *Sci. Rep.*, **7** (1), 2666 (2017).
281. Kaymak V. et al. *Sci. Rep.*, **9** (1), 18672 (2019).
282. Robinson A.P.L. et al. *New J. Phys.*, **10** (1), 013021 (2008).
283. Blanco M., Flores-Arias M.T., Ruiz C., Vranic M. *New J. Phys.*, **19** (3), 033004 (2017).
284. Fedeli L. et al. *New J. Phys.*, **22** (3), 33045 (2020).
285. Passoni M. et al. *Phys. Rev. Accel. Beams*, **19** (6), 061301 (2016).
286. Purvis M.A. et al. *Nat. Photonics*, **7** (10), 796 (2013).
287. Bargsten C. et al. *Sci. Adv.*, **3** (1), e1601558 (2017).
288. Glenzer S.H. et al. *Phys. Plasmas*, **19** (5), 056318 (2012).
289. Curtis A. et al. *Nat. Commun.*, **9** (1), 1077 (2018).
290. Bari M.A. et al. *Laser Part. Beams*, **28** (2), 333 (2010).
291. Lei A.L. et al. *Phys. Rev. Lett.*, **96** (25), 255006 (2006).
292. Ivanov K.A., Shulyapov S.A., Tsymbalov I.N., Akunets A.A., Borisenko N.G., Mordvintsev I.M., Bozh'ev I.V., Volkov R.V., Bochkarev S.G., Bychenkov V.Yu. *Quantum Electron.*, **50** (2), 169 (2020) [*Kvantovaya Elektron.*, **50** (2), 169 (2020)].
293. Torrisi L., Cutroneo M., Cavallaro S. *Ullschmied J. EPJ Web Conf.*, **96**, 01032 (2015).
294. Belyaev V.S. et al. *J. Phys. IV France*, **133**, 507 (2006).
295. Nakashima K., Takabe H. *Phys. Plasmas*, **9** (5), 1505 (2002).
296. Chen H. et al. *Phys. Rev. Lett.*, **105** (1), 015003 (2010).
297. Luo W. et al. *Phys. Plasmas*, **22** (6), 063112 (2015).
298. Breit G., Wheeler J.A. *Phys. Rev.*, **46** (12), 1087 (1934).
299. Burke D.L. et al. *Phys. Rev. Lett.*, **79** (9), 1626 (1997).
300. Li H.-Z. et al. *Opt. Express*, **25** (18), 21583 (2017).
301. Tsymbalov I.N., Gorlova D.A., Bychenkov V.Yu., Savel'ev A.B. *Quantum Electron.*, **49** (4), 386 (2019) [*Kvantovaya Elektron.*, **49** (4), 386 (2019)].